Published in final edited form as:

Nature. 2019 May ; 569(7757): 497–502. doi:10.1038/s41586-019-1199-y.

Distinct modes of cell competition shape mammalian tissue morphogenesis

Stephanie J. Ellis[1], **Nicholas C. Gomez**[1], **John Levorse**[1], **Aaron F. Mertz**[1], **Yejing Ge**[1], and **Elaine Fuchs**[1,*]

[1]Howard Hughes Medical Institute, Robin Neustein Laboratory of Mammalian Cell Biology and Development, The Rockefeller University, New York, USA 10065

Abstract

Cell competition (CC)—the sensing and elimination of less fit "loser" cells by neighbouring "winner" cells—was first described in *Drosophila.* Although proposed as a selection mechanism to optimize tissue and organ development, its evolutionary generality remains unclear. Here, by employing live-imaging, lineage-tracing, single cell transcriptomics and genetics, we unearth two intriguing CC mechanisms that sequentially shape and maintain stratified tissue architecture during mouse skin development. In early embryonic epidermis, winner progenitors within the single-layered epithelium kill and clear neighbouring losers by engulfment. Upon stratification and skin barrier formation, the basal layer instead expels losers through a homeostatic upward flux of differentiating progeny. This CC switch is physiologically relevant: when perturbed, so too is barrier formation. Our findings establish CC as a selective force to optimize vertebrate tissue function, and illuminate how a tissue dynamically adjusts CC strategies to preserve fitness as it encounters increased architectural complexity during morphogenesis.

Main

Not all cells that arise during development contribute to adult tissues, as exemplified by CC studies on *Drosophila* wing epithelial development and germline stem cell niches[1–11]. To date, most vertebrate CC studies have been limited to mouse epiblast and cancerous tissues[10,12–17]. Classically, CC is defined by three features: (1) differences in growth rates among cell populations within a mosaic tissue; (2) active removal of more slowly growing, less fit "loser" cells, dependent upon contact with more fit "winner" cells; and (3) relativity of winner/loser fates that change dependent upon fitness of neighbouring cells.

Increasing attention has been placed on CC in mammalian systems. An elegant description has emerged from studying cultured embryonic stem cells and early post-implantation

*Author for correspondence: fuchs@rockefeller.edu, fuchslb@rockefeller.edu. **Corresponding author.** All correspondence and requests for material should be directed to Elaine Fuchs (fuchslb@rockefeller.edu).

Contributions. SJE and EF conceived the experiments and wrote the manuscript. NCG analysed single-cell data. JL performed all lentiviral infections. AFM assisted in assembly and processing of live-imaging data. YG assisted with library preparation for single-cell sequencing. SJE performed all remaining experiments, data analyses and quantifications.

Competing interests. The authors declare no competing interests.

epiblasts[12–14]. However, the functional significance of CC is not yet clear and it remains unknown whether CC functions in mammals as in *Drosophila* to govern tissue fitness during growth. The prospect becomes particularly interesting for surface epithelia. During evolution from exo- to endo-skeletons, these tissues became stratified to produce protective barriers that constantly rejuvenate from an inner layer of proliferative progenitors.

In mouse embryogenesis, following specification from surface ectoderm, the epidermis expands its surface area >30X to accommodate rapid body-plan growth. The initial progenitor monolayer also stratifies and differentiates to yield a functional, multi-layered permeability barrier at birth. To determine whether CC operates during this process, we exploited prior knowledge that mosaic variation in the *Myc* proto-oncogene triggers CC across a range of proliferative *Drosophila* epithelia[6,18] as well as mouse epiblast[12].

A model to induce CC in skin development

E10.5 mouse epidermis expresses *Myc* and its related isoform, *Mycn*[19] (Extended Data Fig. 1a). Given *Mycn*'s higher expression, we selected floxed *Mycn* mice ($Mycn^{+/fl}$) to generate a mosaic "loser" model. Using *in utero* ultrasound-guided delivery[20], we co-injected amniotic sacs of E9.5 $Mycn^{fl/+}$ or control ($Mycn^{+/+}$) mouse embryos with two equally low-titre lentiviruses (LVs) harbouring either *Pgk-CreRFP* or *Pgk-GFP* (LV-CreRFP/LV-GFP). By E12.5, the LV-packaged genes were integrated and thereafter stably propagated to epidermal progenitor offspring[20] (Extended Data Fig. 1b–c), providing the necessary mosaic embryonic skin to interrogate whether CC is operative and triggered when surrounding epidermal progenitors encounter neighbours that lack a *Mycn* allele.

To test for differences in proliferative capacities, we used comparative growth assays combined with quantitative whole-mount imaging analyses (Fig. 1a,b). By E17.5, RFP $^{+}Mycn^{+/-}$ cells were diminished relative to their initial representation at E12.5 (Fig. 1c). This difference was rooted in a growth disadvantage caused by loss of one *Mycn* allele, since GFP^{+} epidermal cell representation was unchanged between E12.5 and E17.5. Similarly, in $Mycn^{+/fl}$ embryos where RFP^{+} cells were $Mycn^{+/-}$, the RFP:GFP ratio was low compared to $Mycn^{+/+}$ embryos where RFP^{+} cells were wild-type (Fig. 1d). EdU incorporation confirmed that $Mycn^{+/-}$ cells have a proliferative disadvantage (Fig. 1e), thereby fulfilling the first CC criterion.

To assess the second CC criterion, that loser cells are eliminated from tissue dependent upon contact with fitter neighbours, we used time-lapse imaging of E12.5 $R26^{mT/mG}$ embryos ($Mycn^{+/+}$ or $Mycn^{+/fl}$) transduced with *LV-Cre* at E9.5 (Fig. 1f). This approach enabled counting cell death events (Fig. 1g; Extended Data Fig. 2a–d; Supplemental Videos S1–S4) for both GFP^{+} (either $Mycn^{+/+}$ or $Mycn^{+/-}$) and $Tomato^{+}$ cells (always $Mycn^{+/+}$). We asked whether neighbours of dying cells were the same colour (thus the same genotype of the dead cell), or whether dying cells contacted neighbours of both colours.

Quantifications revealed that $GFP^{+}Mycn^{+/-}$ cells in contact with ≥1 $Tomato^{+}Mycn^{+/+}$ neighbour(s) died ~4X more often than either $Tomato^{+}$ wild-type cells contacting only $Tomato^{+}$ wild-type neighbours, or $GFP^{+}Mycn^{+/-}$ cells contacting only $GFP^{+}Mycn^{+/-}$ cells

(Fig.1h). Dying *Mycn*$^{+/-}$ cells also displayed fragmented DNA and active caspase-3 (Fig. 1i–k). These results were not an artefact of LV-Cre infection, as in wild-type embryos transduced with LV-Cre, GFP^{+}*Mycn*$^{+/+}$ cells died no more often than Tomato^{+}*Mycn*$^{+/+}$ neighbours. Moreover, live imaging revealed apoptotic GFP^{+} cells seemingly cleared within the epidermal plane by neighbours (Fig. 1g; see also Extended Data Fig. 2a–e).

Seeking an additional method to quantify death events along clone boundaries, we infected E9.5 *Mycn*$^{+/+}$ control and *Mycn*$^{fl/+}$ embryos with LV-CreRFP and counted TUNEL^{+} corpses in E12.5 embryonic skin. Unlike the uniform expansion of clones seen in fly imaginal discs, rapid clonal intermixing occurs as the mouse epidermis grows, making it difficult to infer a dead/dying cell's neighbours from a single fixed image. However, based on live imaging, a TUNEL^{+} corpse within three cell-lengths of other RFP^{+}*Mycn*$^{+/-}$ cells was likely to represent the recent death of an RFP^{+}*Mycn*$^{+/-}$ cell that had been in contact with RFP^{-} wild-type neighbours. Indeed, compared to controls, RFP^{+}TUNEL^{+} corpses in *Mycn*$^{fl/+}$ embryos were more often found within three cell-lengths of RFP^{+} clones that bordered wild-type cells (Fig. 1k–m; Extended Data Fig. 3c). Thus, *Mycn*$^{+/-}$ "loser" cells appear to die by apoptosis, triggered through a mechanism dependent upon cell-cell interactions with neighbouring *Mycn*$^{+/+}$ "winner" cells.

The third CC criterion is that loser/winner status is relative to the status of neighbouring cells, such that cell death events are not simply due to cell-autonomous loss of a critical gene. To test for this facet of CC, we used *Meox2*^{Cre} to remove one allele of *Mycn* from all cells of the primitive ectoderm[21] (Extended Data Fig. 1c, 3a). In E12.5 backskin of *Mycn*$^{fl/+}$; *R26*^{lslYFP}; *Meox2*^{Cre} animals, TUNEL^{+} cell corpses were minimal, analogous to wild-type and scramble shRNA-transduced embryos (Fig. 1l–m; Extended Data Fig. 3b–c). Strikingly however, upon mosaic knockdown of *Mycn* with 2 different shRNAs in the *Meox2*^{Cre};*Mycn*$^{fl/+}$ background, *Mycn*$^{+/-}$ cells behaved as winners and remained viable, while *Mycn*$^{+/-}$; *Mycn*-shRNA cells died and their TUNEL^{+}RFP^{+} corpses were found proximal to non-transduced *Mycn*$^{+/-}$ cells (Fig. 1l–m, Extended Data Fig. 3c–d). Since complete loss of *Mycn* by K14-Cre-driven deletion resulted in viable animals born with intact epidermis at expected Mendelian ratios (n>5 litters), *Mycn*$^{+/-}$*; Mycn*-shRNA cells were not dying because of cell-autonomous loss of *Mycn*. Rather, in the context of mosaic knockdown, *Mycn*$^{+/-}$*; Mycn*-shRNA cells died dependent upon contact with fitter *Mycn*$^{+/-}$ neighbours. Overall, the shifting of loser/winner fates of *Mycn*$^{+/-}$ epidermal progenitors depending upon neighbours' genotypes fulfilled the third defining characteristic of CC.

Loser cell elimination and clearance

Turning to mechanisms underlying loser elimination, we addressed whether apoptosis is required for CC. We blocked apoptosis throughout mosaic *Mycn*$^{+/-}$ epidermis by co-transducing *K14-rtTA; Mycn*$^{fl/+}$ embryos with low-titre LV-CreRFP and higher-titre LV-*TRE-Bcl2l1*, harbouring a doxycycline-inducible transgene encoding the cell survival protein BCL-XL (Extended Data Fig. 4a,b). Upon induction, most *Mycn*$^{+/-}$ cells (RFP^{+}) were also BCL-XL^{+} and surrounded mostly by BCL-XL^{+}*Mycn*$^{+/+}$ neighbours. TUNEL assays confirmed that elevating BCL-XL abrogated CC-induced apoptosis that otherwise arises in *Mycn*$^{+/-}$ mosaics, and strikingly, the proliferative capacity of *Mycn*$^{+/-}$ cells no

longer differed from their neighbours (Fig. 2a, Extended Data Fig. 4c). Accordingly, the overall growth disadvantage of *Mycn*$^{+/-}$ cells at E17.5 was rescued upon BCL-XL elevation (Fig. 2a). Thus, cell death signalling appears to be required for *Mycn*$^{+/+}$ winner progenitors to exert their competitive advantage over *Mycn*$^{+/-}$ losers for limited space within the basal epidermal layer.

We next asked how dying loser cells are cleared from the embryonic epidermal sheet. Macrophages did not seem responsible, since at E12.5, they were in the dermis and remained so following mosaic *Mycn* manipulation to induce CC (Extended Data Fig. 5a–b). However, adult epidermal cells are known to phagocytose dying cells during the hair cycle, [22] and since embryonic epidermal progenitors express engulfment machinery genes[19], we hypothesized that they might be eliminating dying neighbours. Therefore, using high-titre shRNA transduction (50–80% of basal cells receive the hairpin), we knocked down *Gulp1*, a key component, and induced *Mycn*-dependent CC. Compared to scramble-transduced embryos, more TUNEL^{+} corpses were seen adjacent to CreRFP; *Mycn*$^{fl/+}$ loser cells in *Gulp1*-knockdown epidermis (Fig. 2b). Thus, although engulfment was not required to induce CC, its machinery appeared necessary for neighbours to clear loser cell corpses that arise from CC-induced apoptosis in developing skin.

Evidence for endogenous cell competition

We next addressed whether CC is endogenous to mammalian epidermis development. Although TUNEL assays of wild-type skin rarely identified corpses, we surmised that rapidly cleared death events may be difficult to detect. We therefore dampened the engulfment machinery by transducing wild-type epidermis with *Gulp1*-shRNA at high-titre. Remarkably, this perturbation resulted in littering of numerous TUNEL^{+} epidermal corpses, plausibly representing loser cells that died from endogenous CC (Fig. 2c). Most TUNEL^{+} corpses were RFP^{-}, suggesting that Gulp1 knockdown did not cell autonomously affect viability (Extended Data Fig. 5c). These findings imply that CC is a natural phenomenon, and that winner cells clear the dead/dying “loser” neighbours from the progenitor monolayer through engulfment.

To bolster evidence for endogenous CC, we devised a strategy to identify and characterise emerging winners and losers in wild-type embryos. We hypothesised that winner/loser status might correlate to distinct transcriptional signatures, and reasoned that we could exploit the behaviour of *Mycn*$^{+/-}$ cells as losers to uncover signatures of loser cell identity. Since *Gulp1* data further suggested that in wild-type epidermis, apoptotic cells represent putative losers (Fig. 2c), additional isolation and analysis of pre-apoptotic AnnexinV^{+} cells from otherwise wild-type embryos offered an opportunity to broaden the scope of our transcriptional analyses beyond *Mycn*-dependent CC.

We performed single-cell RNA-sequencing (scRNA-seq) on AnnexinV^{+}; DAPI^{-} (live putative losers), AnnexinV^{-}; DAPI^{-} (putative winners) and *Mycn*$^{+/-}$ epidermal cells (established losers) at E12.5 (Extended Data Fig. 6a–b). We grouped AnnexinV^{+} and *Mycn*$^{+/-}$ cells as “losers” and compared them to AnnexinV^{-} cells (“winners”) to define a

transcriptional signature associated with CC (Fig. 3a; Extended Data Fig. 6d). Strikingly, many genes expressed at low levels in losers encoded ribosomal genes.

Armed with our CC signature, we next performed scRNA-seq on individual K14-H2BGFP$^+$ epidermal cells from wild-type embryos at E12.5 and E17.5 (Extended Data Fig. 7a–e). Each time point clustered distinctly (Fig. 3b). The data supported a single population of unspecified E12.5 progenitors, while at E17.5, distinct sub-clusters emerged encompassing interfollicular epidermis (IFE), differentiating suprabasal and hair follicle progenitors (Extended Data Fig. 7f).

To identify putative losers during embryonic development, we assigned each sequenced cell two scores[23] based on expression of our winner or loser score genes. We then plotted each cell's score and performed a LOESS regression. Cells outside one standard deviation were considered winners (high winner scores, *x*-axis) or losers (high loser scores, *y*-axis; Fig. 3c, Extended Data Fig. 6e). Consistent with CC acting to increase fitness during development, there were fewer losers at E17.5 than E12.5 (Fig. 3c, middle). Moreover, and in contrast to E12.5, loser cells within E17.5 epidermis more often harboured a transcriptional identity associated with differentiation (Fig. 3c, right; Extended Data Fig. 7f).

Developmentally-regulated CC mechanisms

Given these data, we wondered whether maturing epidermis may have cleared out most of its loser cells and therefore no longer require CC. To address this possibility, we first inspected mosaic CreRFP-transduced clonal patches of *Mycn*$^{fl/+}$ epidermis across a developmental time-course. Between E12.5 and E14.5, levels of TUNEL$^+$ neighbours were comparable, indicating that during rapid expansion of the progenitor monolayer, physical contact with wild-type winners led to loser death and engulfment (Fig. 4a). Onward from E15.5 however, basal epidermal progenitors displayed a decline in engulfment gene expression[19] (Fig.4b). Concomitantly, basal losers showed reduced proliferation (Extended Data Fig. 8a) but no signs of apoptosis. These results suggested that at late embryonic time points, either CC is attenuated, or alternatively, CC clears losers by different mechanisms.

In mature epidermis, the innermost (basal) layer maintains proliferative potential and fuels steady outward cellular flux of differentiating cells[24]. Since E17.5 cells transcriptionally classified as losers showed a trend towards differentiation, we interrogated the possibility that late-stage losers are cleared by differentiation and upward efflux from the progenitor layer. Interestingly, while fewer *Mycn*$^{+/-}$ loser cells were retained as K14$^+$ basal progenitors, more losers were found in the K10$^+$ and Flg$^+$ terminally differentiating layers of *Mycn*$^{fl/+}$ epidermis (Fig. 4c; Extended Data Fig. 8b–d). Critically, tissue-wide depletion of *Mycn* did not accelerate epidermal differentiation (Extended Data Figure 8e).

To further address whether this new mode of clearance entails *bona fide* CC, we analysed cell division angles. During normal epidermal development, formation of stratified, differentiating layers is partially fuelled by orienting >60% basal progenitor spindles perpendicularly to the basement membrane, such that one daughter cell remains within the progenitor pool while the other becomes suprabasal and fated to terminally differentiate[25].

Intriguingly, in E15.5 mosaic skin, spindle orientations became skewed towards perpendicular divisions within loser *Mycn*$^{+/-}$ clones compared to wild-type counterparts (Fig. 4d, Extended Data Fig. 8f). Additionally, knockdown of *Lgn,* required for asymmetric cell division (ACD) and differentiation in developing skin[25,26], resulted in increased basal layer retention of *Mycn*$^{+/-}$ cells at E17.5 (Fig. 4c).

Most revealing and in line with roles for both ACD and CC in promoting loser basal cell clearance, perpendicular spindle angling was higher in *Mycn*$^{+/-}$ progenitors that were surrounded by wild-type neighbours at E15.5 (Fig. 4e). Although modest, no such correlation was found with control-labelled clones, suggesting that this mode of eliminating less fit cells may also be dependent upon direct contact between winner and loser cells, one of the hallmarks of CC.

Functional consequences of CC

Finally, we tackled the physiological relevance of CC. To this end, we exploited the fact that apoptotic/engulfment-mediated CC was efficiently blocked in BCL-XL^{+} embryos and then assayed for epidermal barrier function, which in wild-type embryos is operative by E17.5[27]. Tight junctions (TJs), critical barrier components of the upper epidermal layers, showed signs of compromise: cortical localization of TJ components Claudin-1 and ZO-1 was diminished in E17.5 BCL-XL^{+} compared to control embryos (Fig. 5a–b). Additionally, as judged by trans-epidermal water loss (TEWL)[28] assays, blocking apoptotic-mediated CC in BCL-XL^{+} embryos led to greater and more variable TEWL compared to control embryos (Fig. 5c, top; Extended Data Fig. 9b). Moreover, upon enhancing CC through mosaic manipulation of *Mycn* expression, TEWL was even further increased in BCL-XL^{+} embryos; this increase was not observed when apoptotic-CC was unperturbed (Fig. 5c, bottom). Although we cannot unequivocally exclude BCL-XL roles other than CC during emergence of barrier function, our results suggest that BCL-XL acts directly on CC (Extended Data Fig. 4e), and that when apoptotic-mediated CC is abrogated, basal progenitors cannot establish the skin's barrier as efficiently as when CC is intact.

Interestingly, consistent with a developmental switch in CC mechanisms, TJ and TEWL differences disappeared by birth (Fig. 5d). Together, these data suggest that by equipping the tissue with sequential death→differentiation loser cell clearance mechanisms, the epidermis ensures that if the first mechanism is defective, an effective barrier can still be established by birth. To further test this possibility, we interrogated how CC impinges on clonal expansion dynamics during epidermal growth and differentiation via an *R26*^{Confetti}-based lineage tracing strategy (Extended Data Fig. 9c–d). We interrogated clones that were either wild-type, BCL-XL^{+} or *Mycn*$^{+/-}$ and measured the impact on growth/differentiation when CC was either accentuated (*Mycn*$^{+/-}$) or intercepted (BCL-XL^{+}).

Quantifications revealed that compared to wild-type clones, both *Mycn*$^{+/-}$ (pink) and BCL-XL^{+} (teal) clones showed significant reductions in clone size (Extended Data Fig. 9e), not unexpected given the slight decrease in proliferation we observed for both genotypes early in skin development (Fig. 1e; Extended Data Fig. 4d). However, closer inspection revealed differences in basal:suprabasal distributions of *Mycn*$^{+/-}$ versus BCLX-L clones (Figs. 5e,f;

Extended Data Fig. 9f). In line with their loser status, *Mycn*$^{+/-}$ clones were small and more differentiated compared to wild-type counterparts, but by E17.5, most clones still had basal cells. By contrast, many BCL-XL^{+} clones consisted of fully differentiated cells, corroborating our assertion that in absence of apoptotic CC, differentiation becomes a more prominent mechanism to rid the basal layer of less fit progenitors.

Discussion

In summary, we unearthed a physiologically relevant CC circuit that operates in a mammalian tissue. In early stages of mouse skin development, when epidermis is single-layered, arising loser cells trigger fitter neighbouring cells to kill and engulf them. This process depends upon loser-winner contact and occurs even in wild-type epidermis, as revealed by our transcriptomic studies and by the presence of littered corpses when engulfment is blocked. In this way, the early embryonic mouse epidermis appears to have retained evolutionary CC mechanisms similar to those in the fly.

The enrichment of ribosomal genes in our CC transcriptional signature provides a further intriguing parallel with classic *Drosophila* studies[1–3,29], and fuels the idea that regulatory control at the level of translation/protein synthesis is a determining feature of cell fitness during growth. This notion also potentially explains why our signature does not include genes from pathways implicated in CC that may be regulated post-transcriptionally. The developmental switch from apoptosis/engulfment-mediated CC to ACD/differentiation-mediated CC (Extended Data Fig. 10) sets mammalian epidermis apart from other CC systems studied to date. The ability to flux loser progenitors from the basal layer via differentiation provides a backup mechanism to eliminate losers not cleared earlier by apoptosis/engulfment. Thus, the stratified, differentiating epidermis of mammalian skin is endowed with an evolutionary advantage that single-layered epithelia lack.

As evidence for CC as a tumour suppressive mechanism mounts[15,16,30], our findings have implications for growth control not only in healthy tissues but also in disease. In human skin, it has been posited that spatial relationships and competitive behaviours amongst clones may act to impede malignant progression[31], especially in light of the large mutational burden that accumulates in phenotypically normal tissue during postnatal life[32]. Indeed, in mouse models, wild-type epidermal cells can promote regression of pre-cancerous overgrowths[33]. It is tempting to speculate that elimination of unfit cells in these contexts occurs through one or both mechanisms of CC that we describe. As the field learns more about fitness-sensing mechanisms within tissues, it should become clearer whether CC might be harnessed for future therapeutic avenues.

Methods

Mouse lines and lentiviral constructs

Mice were housed in the Association for Assessment and Accreditation of Laboratory Animal Care International (AAALAC)-accredited Comparative Bioscience Center at the Rockefeller University. All procedures were performed using Institutional Animal Care and Use Committee (IACUC)-approved protocols and in accordance with the procedures

outlined in the Guide for the Care and Use of Laboratory Animals. The following previously generated mouse lines were used in this study: *Rosa26*^{mTmG}(ref [34]), *Rosa26*$^{Brainbow2.1}$(ref [35]), *Mycn*$^{fl/fl}$ (ref [36]), *Keratin14*^{rtTA}, *Meox2*^{Cre} (ref [21]), *Rosa26*^{EYFP} (ref [37]). All strains were maintained in a mixed CD1 background. For most experiments, heterozygous *Mycn*$^{fl/+}$ females were bred to either CD1 or mixed background WT males to generate *Mycn*$^{fl/+}$ animals as well as *Mycn*$^{+/+}$ littermates as controls. Embryos were injected with lentivirus at 9.5 days post coitum (dpc) as previously described[20]. To induce recombination of transgenic cassettes, the following lentiviruses were injected: *LV-Cre*[20], *LV-Cre*^{ERT226}, *LV-nls-iCreH2BRFP*[20], or *LV-nls-iCre-nlsGFP*. To activate *LV-Cre*^{ERT2} activity at E14.5 in *R26*^{mtmg}/*Mycn*$^{fl/+}$ experiments as shown in Figure 3, pregnant moms were given a single 2% tamoxifen dose by oral gavage at 14dpc. shRNAs clones were obtained from The RNAi Consortium (TRC) shRNA library (Sigma), present in the pLKO.1-puro vector and tested for knockdown efficiency in primary mouse keratinocytes. The puro cassette was swapped out for an H2B-RFP marker prior to transfection into 293-FT cells for high titre lentivirus production. All experiments with *Meox2*^{Cre} were in a *Rosa26*^{EFYP} background, allowing us to exclude animals from significant mosaicism from our analysis (see Extended Data Fig. 3a). To make TRE-*Bcl2l1*, myc epitope-tagged mouse *Bcl2l1* cDNA (Origene clone RC201314) was PCR-amplified and inserted into NheI and EcoRI restriction sites of a pLKO vector modified to contain the inducible tetracycline response element such that BCL-XL expression could be robustly induced by doxycycline treatment.

shRNA sequences

Mycn shRNA #1 (TRCN0000042524) - CAGTTGCTAAAGAAGATCGAA

Mycn shRNA #2 (TRCN0000042525) - CCTCACTCCTAATCCGGTCAT

Gulp1 shRNA #1 (TRCN0000101261) - CCAGCTTCATAGAATATCATT

Gulp1 shRNA #2 (TRCN0000101262) – GCCAGCTTCATAGAATATCAT

Lgn shRNA 1617 (TRCN0000028914) – GCCGAATTGGAACAGTGAAA

Scramble shRNA (SHC002) – CAACAAGATGAAGAGCACCAA

Immunofluorescence and Antibodies

For all immunofluorescence experiments embryos were fixed for 1 hour in 4% paraformaldehyde. For wholemount imaging of backskin at all time points except E12.5, back skin was dissected from the animal and cut into four quadrants. E12.5 embryos wholemounts were kept intact throughout the whole staining and imaging procedure. Following fixation, samples were permeabilized in 0.3% PBS-Triton for 3–4 hours at RT, and blocked in blocking buffer (5% donkey serum, 2.5% fish gelatin, 1% BSA, 0.3% Triton in PBS) for 1 hr at RT. Primary antibodies were incubated overnight at 4°C, samples were washed 3–4 hours in PBS-Triton at room temperature, and secondary antibodies were incubated overnight together with DAPI (to label nuclei). Whole embryos and back-skins (post E12.5) were mounted in Prolong Diamond Antifade Mountant with DAPI (Invitrogen) for imaging. For sections at E17.5 backskin was cut into strips, embedded and frozen in

OCT (Leica), and sectioned with a Leica cryostat (12μm sections). EdU was administered via intraperitoneal injection of pregnant females, which were then sacrificed and embryos dissected from the uterine horns 45 minutes post injection. EdU labelling of embryos was performed using the Click-iT Alexa Fluor 647 Imaging kit (Thermofisher) according to manufacturer's instructions, between application of the primary and secondary antibodies. For TUNEL labelling, the Click-iT TUNEL Alexa Fluor 647 Imaging Assay for microscopy & HCS kit (Invitrogen) was used. Our protocol was according to the manufacturer's instructions, except that samples were incubated in TdT for 2 hours at 37°C on an orbital shaker. A DNAseI-treated sample was used as an initial positive control to confirm that efficient TUNEL labelling in the basal epidermis. Due to increased tissue thickness, to obtain efficient TUNEL labelling at E17.5, backskin was incubated overnight at 4°C in dispase to facilitate removal of the dermis prior to TUNEL labelling. Antibodies used were as follows: Rat anti-RFP (Chromotek, 5F8; 1:1000), Rabbit anti-RFP (MBL, PM005; 1:1000), Chicken anti-GFP (Abcam, ab13970; 1:1000), Rat anti-E-cadherin (M. Takeichi; 1:50), Rabbit anti-keratin14 (Fuchs lab; 1:200), Rabbit anti-keratin10 (Covance, 1:500), Rabbit anti-Cleaved-Caspase3 (Cell Signalling 9661, 1:200), rat biotinylated anti-CD45 (Biolegend, 5530; 1:200), rabbit anti-myc epitope [71D10] (Cell Signalling, 2278; 1/:200), rabbit anti-survivin (Cell Signalling, 71G4B7, 1:200), rabbit anti-Involucrin (Biolegend, PRB-140C, 1:1000), rabbit anti-Filaggrin (Fuchs lab, 1:500), rabbit anti-Loricrin (Fuchs lab, 1:500), and goat anti-P-cadherin (R&D, AF761, 1:200), rat anti-CD104 (beta4-integrin; BD Biosciences, 1:200), rabbit anti-Claudin 1 (Cell Signaling, D5H1D, 1:100), and rabbit anti-ZO-1 (Zymed, 2533938; 1:200). All secondary antibodies used were raised in a donkey host and were conjugated to one of Alexafluor488, Rhodamine, or AlexaFluor647 (Jackson ImmunoResearch Lab; 1:500). Rhodamine phalloidin (Life Technologies) was used to label F-actin (1:500). 4',6-diamidino-2-phenylindole (DAPI) was used to label nuclei (1:5000).

Microscopy and Live Imaging

Live imaging was carried out based on the protocol used in Ouspenskaia et al[38]. E12.5 mouse embryos were placed on their sides in a 35-mm Lumox-bottom dish (Sarstedt). Each embryo was immobilized with a custom built holder and further stabilized in an agarose solution comprised of 2% low-melting SeaPlaque Agarose (Cambrex) in a solution of epidermal culture medium. After equilibrating at 37°C and 5% CO2 for ~2 hr, imaging was then performed on a custom-modified inverted spinning disk confocal system (Andor) at 12 min intervals for up to 24 hr (488 and 561 nm laser beams, 20× air objective (N.A.=0.75). Time-lapse images were acquired with a Zyla cCMOS camera (Andor). 3–4 regions were filmed from each embryo. During imaging, the embryo was maintained at 37°C and 5% CO2. Acquisition was controlled through iQ software (Andor).

All wholemount immunofluorescence images were acquired using a Zen-software driven Zeiss LSM 780 inverted laser scanning confocal microscope and either a 20x air objective (NA=0.8), a 40x water immersion objective (NA=1.2), or a 63x oil immersion objective (NA=1.4).

Images of epidermal cryosections were acquired using a Zeiss Axio Observer.Z1 epifluroescent/brightfield microscope with a Hamamatsu ORCA-ER camera, an ApoTome.2

slider (to reduce light scatter in z), and controlled via Zen software. All images were assembled and processed using ImageJ.

Image Processing and Analysis

Comparative Growth Assays—Maximum projection images were assembled from wholemount images of embryos infected with LV-CreRFP and LV-GFP at both E12.5 and E17.5 timepoints. Images were segmented in ImageJ to identify and count the number of GFP^+ nuclei and RFP^+ nuclei as a proportion of the total number of $DAPI^+$ nuclei (%RFP^+ and %GFP^+). To obtain the ratios shown in Fig. 1d and 2a, the ratio of %RFP^+ to %GFP^+ cells was calculated at E12.5 and E17.5. The ratio at E17.5 was normalized to that of E12.5 to determine if representation of RFP+ changed relative to green. In WT embryos, the ratio of RFP:GFP remains relatively stable over developmental time.

Cell Proliferation Assays—In most cases (all except Extended Data Figure 8a, where mitotic events were measured by looking for chromosome condensation visible via DAPI staining), proliferation was inferred from the incorporation of labelled nucleotide analogues following a 45-minute EdU pulse. To assess subtle differences in proliferation that occur as a result of cell competition (as in Fig. 1e, 2a), measurements were made paired, directly comparing the EdU incorporation of $CreRFP^+$ cells to that of $CreRFP^-$ neighbours in the same region. This is especially important because, distinct from mosaic approaches in Drosophila, the lentiviral technique does not allow for twin-spot analyses. However, in cases where we more generally assessed for changes in proliferation, we pooled EdU incorporation measurements between multiple animals of the same genotype, and performed unpaired analyses (as in Extended Data Fig. 3b and Extended Data Fig. 4d).

Live Imaging Processing and Analyses—In ImageJ, videos and single time-point images were processed by averaging three adjacent z-stack images and then applying a Gaussian blur of radius 1 pixel (0.27 μm). Death events were manually scored. For each putative cell death event, the entire z-stack acquired was scanned through to rule out extrusion of cells into other planes (for an example see Extended Data Fig. 2e).

Quantification of Neighbouring $TUNEL^+$ Events—Maximum projection images featuring the basal plane of the epidermis from LV-CreRFP+ transduced embryos were assembled in ImageJ. The RFP+ was thresholded to allow unambiguous detection of RFP^+ nuclei. RFP^+ cells within 3 cell lengths (as determined by DAPI signal) were classified as having $TUNEL^+$ neighbours. The total number of RFP^+ cells with $TUNEL^+$ neighbours was then plotted as a fraction of the total number of RFP^+ cells.

Spindle Angle Quantification—Backskin from E15.5 embryos was dissected and stained for survivin, a reliable marker of spindle orientation during mitosis. From wholemount images, the xyz-position of the start and end of each surviving-marked spindle was recorded, and using trigonometry, the spindle angle could be inferred. For every mitotic cell, the number of neighbours, either GFP^+ or RFP^+, was also recorded for future correlation analysis, which was performed using Prism8 (Graphpad).

Tight Junction Analyses—To quantify the recruitment of tight junction markers, ImageJ was used to measure the integrated density (a well established method of measuring fluorescence intensity that accounts for differences in area) of either Claudin-1 or ZO-1 signal in the suprabasal layer of the skin (labelled by F-actin staining).

Transepidermal Water Loss Assay

A Tewameter TM300 (Courage + Khazaka electronic GmbH) was used to take measurements from the backskin of E17.5 embryos and P0 neonates. To adjust for the relative small size of these animals, an adapter was used on the probe head such that the area of measurement was ~2mm^2. We selected the shoulder region (just posterior to the ear) for analysis such that two measurements could be performed on each animal in areas infected with the *tre-Bcl2l1* lentivirus at similar levels. E17.5 embryos were incubated in PBS and thus were gently dried off with a kim wipe prior to measurements. Every measurement represents an average of 5 individual subsequently recorded measurements at the probe head. It takes about 30 seconds for the measurements to stabilize such that the error between the 5 measurements was minimized. These stable values were recorded as data points. The absolute value of the difference between the two values recorded from the left and right sides of each animal was used as an index of variability. Genotyping was performed following the experiment such that we were blinded to genotypes during measurements.

Lineage Tracing Strategy for Assessment of Clonal Growth Dynamics

To induce *Cre^{ERT2}* activity for *R26^{Confetti}* experiments, pregnant mothers were treated with 100ul of 2% tamoxifen (Sigma) dissolved in corn oil (Sigma) by intraperitoneal injection at 11.5dpc. Embryos were dissected from the sacrificed mother at 14.5dpc and 17.5dpc. Dissected E17.5 backskins was stained for GFP, RFP, and P-cadherin (to label basal cells) and/or E-Cadherin, mounted dermis side down, and entire pieces of backskin were imaged such that all labelled clones in the population were captured via laser scanning confocal microscopy. Overall clone size was manually counted at E17.5 (Extended Data Fig. 9e). The basal layer was labelled with P-cadherin, allowing determination of cells within each clone that remained basal versus suprabasal (Fig. 5e, f; Extended Data Fig. 9f). E-cadherin could also be used to distinguish basal cells from all other cells due to their distinctive morphology compared to all epidermal cells at E17.5. Induction efficiency was low such that clonal labelling density was sparse, affording us confidence that we were always observing single clones rather than merged clones of the same colour that may have intermixed as due to clonal dispersion. Any clones of the same colour that were found within ~500μm of one another were excluded from analysis. Membrane-bound CFP and cytoplasmic YFP could be detected with a GFP antibody and distinguished from one another by their subcellular localization. Consistent with prior reports, we rarely observed GFP labelled clones[35]. YFP, CFP, and RFP were found in roughly equal proportions throughout the backskin (Extended Data Figure 9d).

FACS and Quantitative Real-Time PCR

For scRNA-seq, single cell suspensions were obtained from either E12.5 or E17.5 K14-H2B-GFP/+ mice; single epidermal cells were sorted into 96-well plates sorting for lineage

negative ("lin$^-$") GFP$^+$ cells using a BD FACSAriaII. CD45 (biotinylated rat anti CD45, BD Biolegend, 1:200), CD117 (biotinylated rat anti CD117/c-kit, Biolegend, 1:200), CD31 (biotinylated rat anti-CD31/PECAM, Bioscience, 1:200), and CD140a (biotinylated rat anti-CD140a, Biolegend, 1:200) were used as lineage negative markers (to exclude immune cells, melanoblasts, endothelium, and fibroblasts, respectively). All lin- were detected with a strepdavidin-conjugated PeCy7 secondary (Biolegend, 1:500). To obtain samples required to generate our cell competition signature, K14-H2B-GFP cells were further stained for AnnexinV (Alexa Fluor 568 conjugated; ThermoFisher Scientific, 1:200); 2 96-well plates of single cells were obtained for each lin-/GFP$^+$/AnnexinV$^+$ (losers) and 2 plates worth of lin-/GFP$^+$AnnexinV$^-$ (winners). *Mycn*$^{+/-}$ epidermal cells (losers) were obtained from E12.5 *K14-H2B-GFP/+; Mycn*$^{fl/+}$ embryos transduced at low titer with LV-*CreH2B-RFP* and sorted for lin$^-$/GFP$^+$/RFP$^+$. Each sample comprised single cells from at least 3 embryos per genotype.

To measure *Mycn* levels in *Mycn*$^{+/-}$ cells, E12.5 basal epidermal cells were isolated from embryos infected with *LV-nlsCreH2BRFP*. Single cell suspensions were stained with anti-CD49f/alpha6-PE/Cy7 (Biolegend, 1:1000) and/or AnnexinV (Alexa Fluor 568 conjugated, Life Technologies, 1:200) and sorted using a BD FACSAriaII. RNA was isolated in Trizol from alpha6hi, RFP+, lin- cells using the Direct-zol RNA Miniprep Plus kit (Zymo Research). CD45 (biotinylated rat anti CD45, BD Biolegend, 1:200), CD117 (biotinylated rat anti CD117/c-kit, Biolegend, 1:200), CD31 (biotinylated rat anti-CD31/PECAM, Bioscience, 1:200), and CD140a (biotinylated rat anti-CD140a, Biolegend, 1:200) were used as lineage negative markers (to exclude immune cells, melanoblasts, endothelium, and fibroblasts, respectively). All lin- were detected with a strepdavidin-conjugated FITC or APCCy7 secondary (Biolegend, 1:500). Equivalent amounts of RNA were reverse-transcribed by SuperScript VILO cDNA Synthesis Kit (Invitrogen). cDNAs were mixed with indicated primers and Power SYBR Green PCR Master Mix (AppliedBiosystems), and quantitative PCR (qPCR) was performed on a Applied Biosystems 7900HT Fast Real-Time PCR system. cDNAs were normalized to equal amounts using primers against *Ppib*. Primer sequences were as follows: *Mycn* forward: 5'-CCTCCGGAGAGGATACCTTG-3'; *Mycn* reverse: TCTCTACGGTGACCACATCG; *Myc* forward: 5'-CAGCGACTCTGAAGAAGAGCA-3'; *Myc* reverse: 5'-TTGTGCTGGTGAGTGGAGAC-3'; *Ppib* forward: 5'-GTGAGCGCTTCCCAGATGAGA-3'; *Ppib* reverse: 5'-TGCCGGAGTCGACAATGATG-3'.

Single-cell RNA Sequencing Library Preparation

Single cell RNA-seq libraries were prepared using the Smart-seq2 protocol[39] with a few modifications. Briefly, plates were thawed on ice and incubated for 3 min at 72C to lyse cells. Reverse transcription (4U/ml Maxima H- transcriptase), template switching reaction and PCR pre-amplification (15 cycles) were performed according to the manufacturers' protocol. PCR products were cleaned up using 0.8X AMPure XP beads (Beckman Coulter). The cDNA library quality was assessed by qPCR for primer pairs targeting the housekeeping gene, *Gapdh*. Samples showing high Ct value (>35 cycles) or having no PCR amplification were excluded from downstream analysis. 50–100pg of each cDNA library was used for

generating Illumina sequencing libraries using a Nextera XT DNA library preparation kit (Illumina). After the final PCR amplification step, samples were pooled and cleaned by 0.9X AMPure XP beads. The pooled sequencing libraries were sequenced in the RU genomics facility on an Illumina Nextseq500 instrument using the High Output 75 PE kit.

Single-Cell RNA-Sequencing Analysis

1) Read alignment and gene quantification—Paired-end sequencing reads from single cell RNA-seq libraries were aligned to the mouse transcriptome Gencode M18 (GRCm38.6,mm10) using Salmon[40]. Transcripts counts were collapsed into gene quantifications using the tximport[41] package in R. For downstream analyses, cells with < 3000 genes detected and genes expressed in < 5 cells were discarded.

2) Identification of highly variable genes—We combined all single cell data sets (E12.5 WT, E12.5 LV, E17.5, AnnexinV$^+$, AnnexinV$^-$, E12.5 *Mycn*$^{+/-}$) to create a union set for identifying highly variable genes (HVG). We utilized a statistical model[42] incorporating ERCC spike-ins to identify biological variability from technical noise in our experiments. We identified 8295 HVG, relative to technical variation (ERCC spike-in), and a false discovery rate value less than 0.1 that were deemed to be highly variable. All subsequent analyses were performed using these genes within the Seurat scRNA R toolkit[43].

3) Identification of Cell Competition (CC) signature—To identify a CC signature we pooled *Mycn*$^{+/-}$ and WT AnnexinV$^+$ cells to create a single “loser” identity and performed differential expression analysis comparing to AnnexinV$^-$ cells (“winners”). Genes were considered to be significantly different if they had an adjusted p-value of < 0.05 (Extended Data Fig. 6). Genes with higher expression in “losers” were termed Loser genes, and those with higher expression in “winners” were termed Winner genes.

These gene groups were then used to assign a Loser and Winner score to each cell in WT E12.5 and E17.5 cells[23,43] and plotted. Because of the inverse relationship between expression of Loser and Winner genes, we multiplied the Winner Score by −1 to ensure that the axes were consistent (low scores are associated with winners while higher scores are associated with losers). We then performed a LOESS regression and plotted a 1 standard deviation interval using the R function loess.sd. Cells above 1 standard deviation were considered to be losers while those below were called as winners.

4) Clustering and tSNE of E12.5 and E17.5 cells—Raw count data from E12.5 and E17.5 for HVG was imported into a Seurat and log-normalized using the default parameters. We then scaled the data regressing batch, and cell cycle effects from the subsequent analyses. We identified 15 significant PCA dimensions as determined by Jack Straw analysis (Extended Data Figure 7). These components were then tSNE clustered with a resolution of 0.6 within Seurat.

5) Subclustering of E17.5 cells—E17.5 cells were subsetted from the original scaled data and tSNE clustered using 9 significant PCA dimensions (as described above) and a resolution of 0.6. The algorithm identified two primary clusters E17.5 Interfollicular Epidermis (IFE) and HF Progenitors based on the expression of cell type specific genes.

Further analysis using epidermal suprabasal lineage-specific gene *Krt10* allowed us to identify a third distinct cluster, which we classified as Suprabasal cells.

Statistics and Study Design

In general, all experiments were repeated on at least 2 litters per experiments. All experiments were designed such that there were always WT littermate controls. All datasets generated were tested for Normal distributions using Prism 7/8 (Graphpad) and all datasets that failed this test were subject to non-parametric tests for further analysis. All statistical tests performed are as indicated in the figure legends.

Data availability.

Single cell RNA sequencing data that support the findings of this study are deposited in Gene Expression Omnibus (https://www.ncbi.nlm.nih.gov/geo/) with the accession number GSE128241. RNA sequencing data shown in Figure 4b and Extended Data Figure 1a were extracted from the study by Asare et al[19] and were previously deposited in GEO with the accession number GSE75931. All other data are in the manuscript, supplementary materials and source data or available from the corresponding author upon reasonable request.

Extended Data

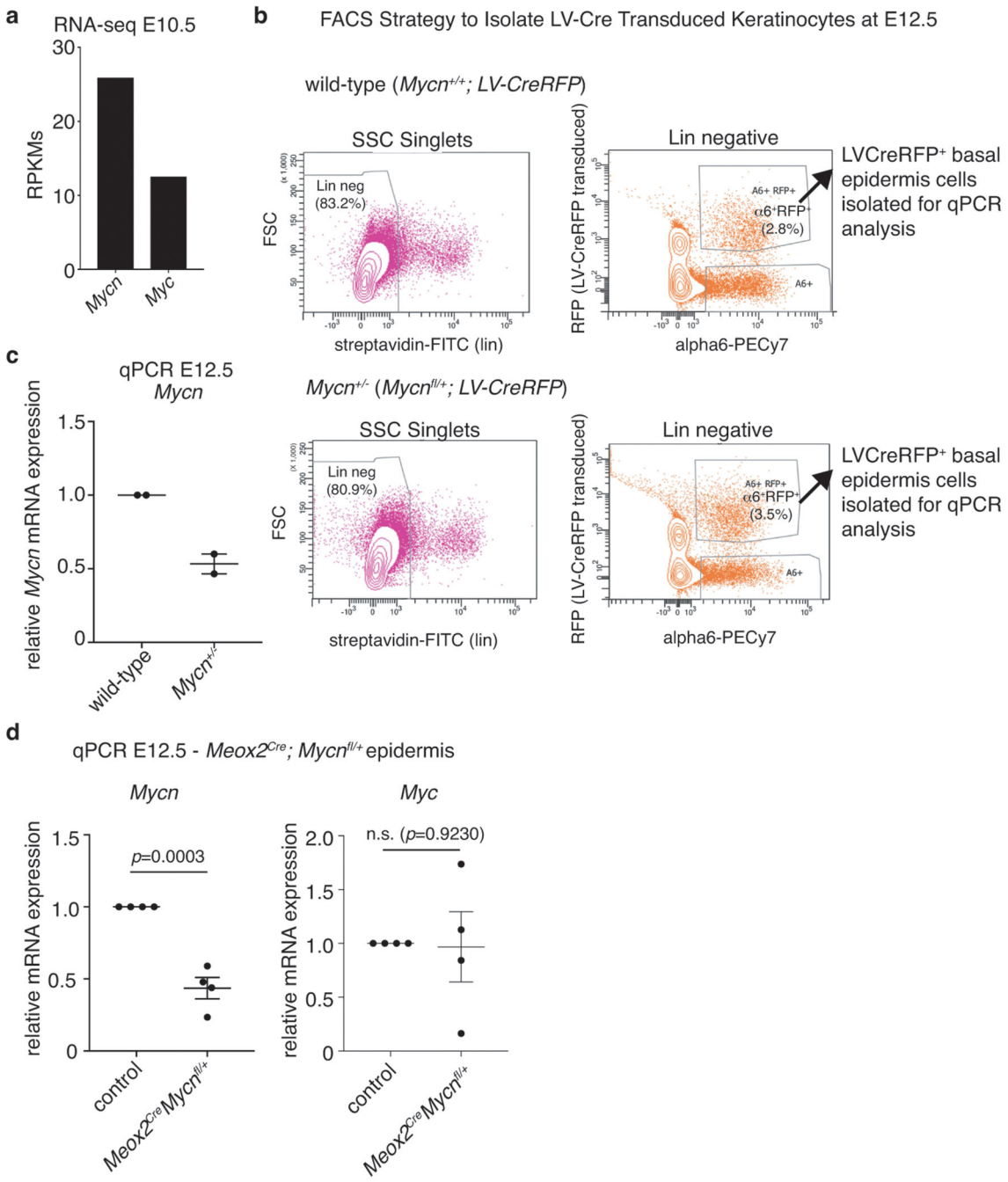

Extended Data Figure 1. *Mycn* is expressed in single-layered embryonic epidermis and its expression is halved in both genetic model *Mycn*$^{fl/+}$; *LV-CreRFP* and *Mycn*$^{fl/+}$; *Meox2*^{Cre} with no compensatory upregulation of *Myc*.

a, *Mycn* and *myc* expression in E10.5 epidermis by RNA-seq[19]. *Mycn* is expressed at higher levels than myc. **b** Fluorescence activated cell sorting (FACS) strategy to isolate LV-CreRFP-transduced wild-type and *Mycn*$^{+/-}$ basal keratinocytes from E12.5 embryonic skin. **c-d,** quantitative polymerase chain reaction (qPCR) revealed that transcript levels were halved in *Mycn*$^{+/-}$ cells compared to wild-type at E12.5 using both LV-Cre (n=2) and *Meox2*^{Cre} (n=4, unpaired two-tailed t-test). No significant compensatory change in levels of

Myc mRNA levels was observed. Embryos of each genotype within a single litter were pooled together for cDNA collection. This was repeated to generate 2 biological replicates per genotype. Data=mean ±S.E.M.

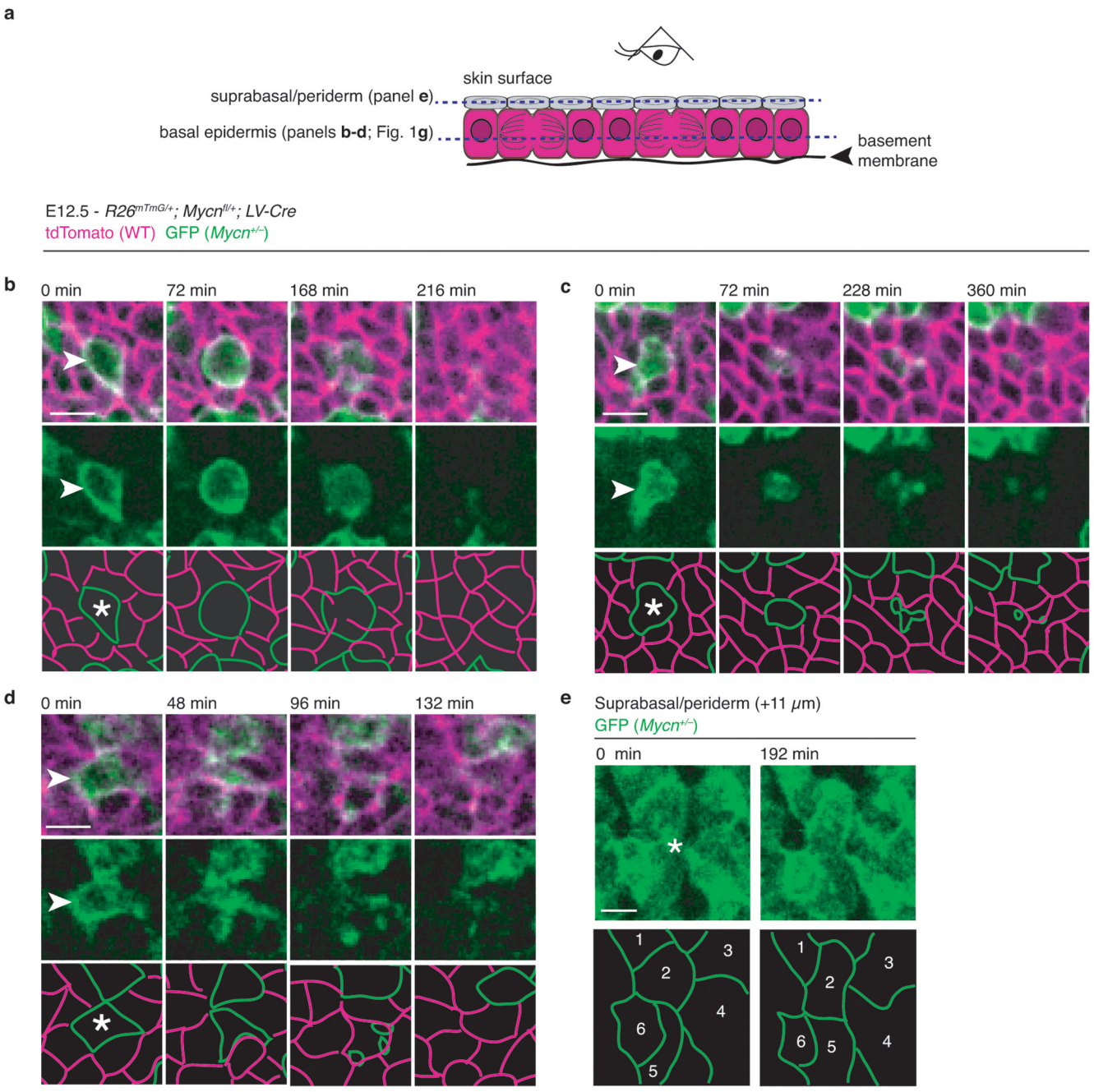

Extended Data Figure 2. Live imaging reveals that loser cell death is preceded by increased contact with WT cells and suggests engulfment mediates clearance of loser cell corpses.

a, Schematic showing planes imaged in time-lapse microscopy experiments. **b-d,** Extracted images showing frames from Supplemental Videos S2–S4. Dying cells GFP^{+}*Mycn*$^{+/-}$ cells are marked with an arrowhead in the first frame of fluorescence images (top two rows) and by an asterisk in the traced panels (bottom row). Wild-type cells are RFP^{+}. **e**, Images from the suprabasal plane extracted from the first and last time point of Supplemental Video S1, and corresponding to the still images shown in the first and last panels of Figure 1g. The asterisk marks the position of the dying cell 11μm below. No new cells enter the suprabasal

plane through the time course of the video supporting the conclusion the cell dies and is eliminated within the plane of the epidermis and not extruded to the suprabasal planes. Scale bar = 10μm.

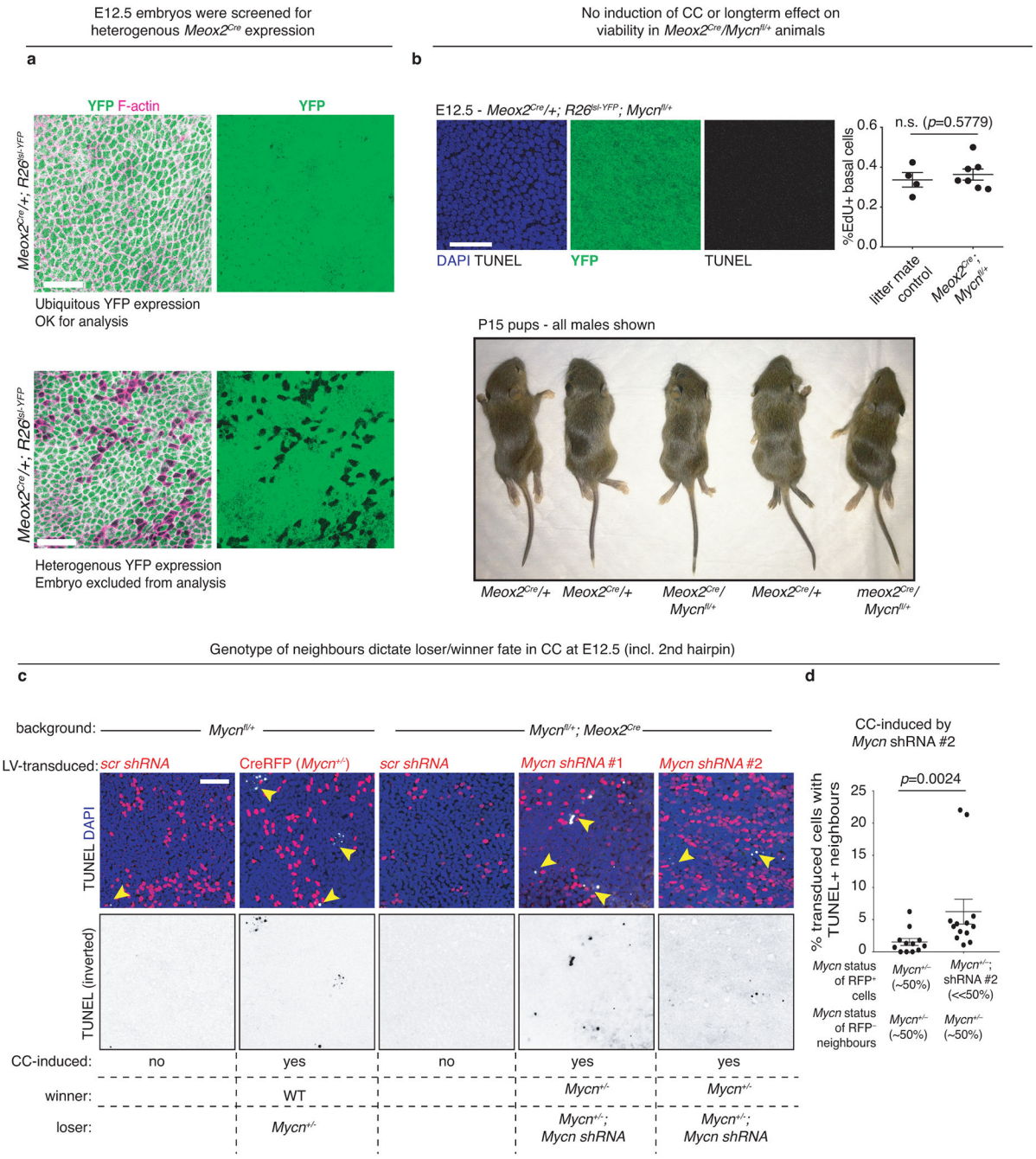

Extended Data Figure 3. A genetic model to switch the fate of *Mycn*$^{+/-}$ epidermal cells from losers to winners.

a, *R26*^{YFP} reporter for Cre activity shows undesired mosaicism in some embryos, which were prescreened and excluded from further analysis. All *Meox2*^{Cre} embryos in our study were subjected to this analysis. **b**, TUNEL stain of *Mycn*$^{+/-}$*; R26*^{YFP} embryos revealed neither TUNEL labelling in regions of ubiquitous Cre activity (as indicated by YFP expression), nor any marked differences in proliferation as assayed by EdU incorporation (n=images analysed from each genotype, control n=4, MeoxCre n=7, two-tailed unpaired t-

test). There also was no discernable impact on postnatal viability or growth (P15 males shown in bottom panels, genotypes as indicated). **c-d**, Extended fields of view (**c**) from images shown in Figure 1m of wholemount E12.5 backskins stained for DAPI (nuclei, blue), RFP(transduced cells, red) and TUNEL (dying cell corpses, white; see arrows) for each of the indicated genotypes. An additional representative image and quantification is also shown for a second *Mycn* shRNA, **d** (*n*=number of images quantified from 2 litters per genotype; $Mycn^{+/-}$/ $Mycn^{+/-}$ *n*=13, $Mycn^{+/-}$/$Mycn^{+/-}$;sh*Mycn* #2 *n*=12, two-sided Mann-Whitney test). Data=mean ±S.E.M, scale bars = 50μm.

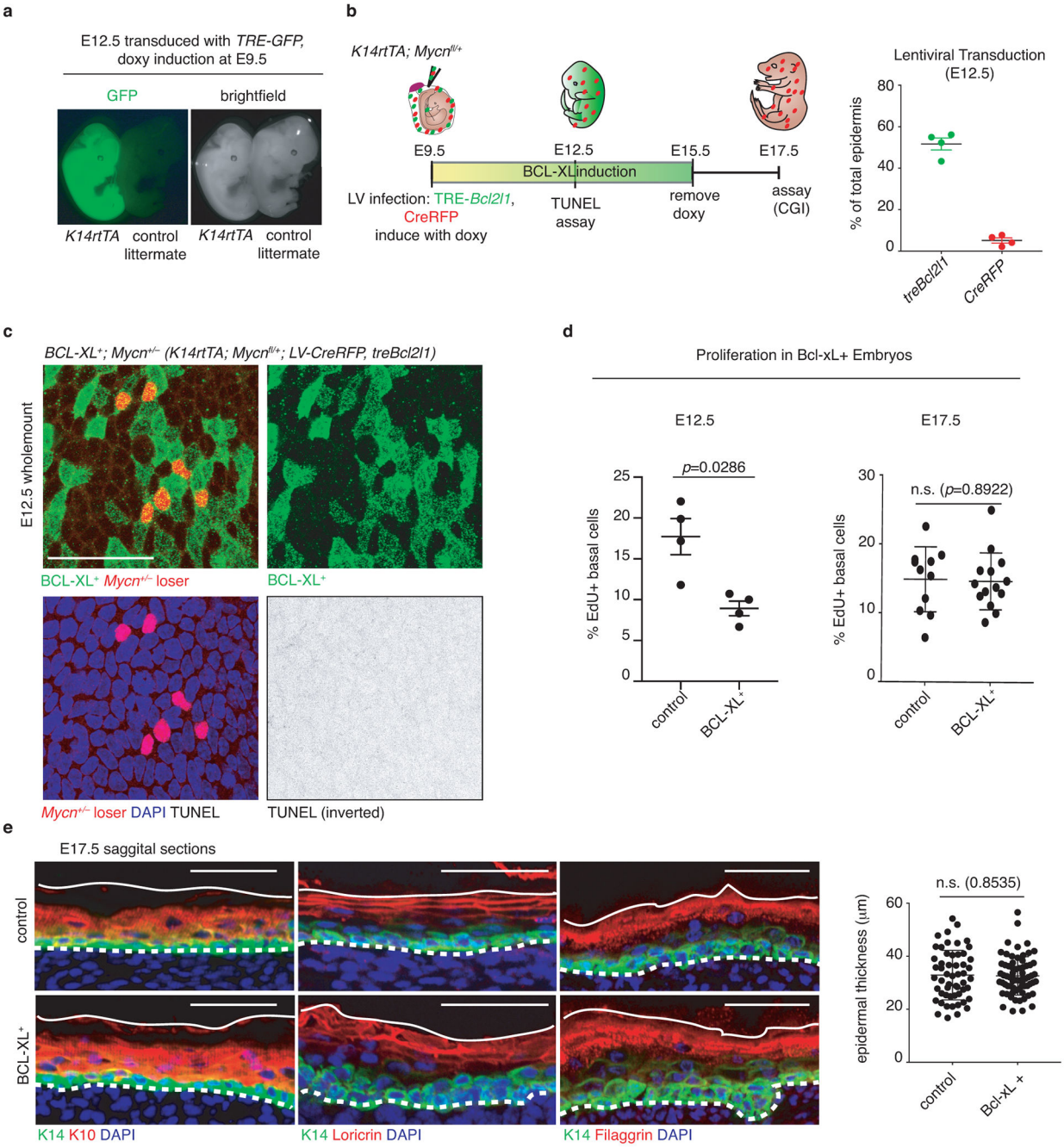

Extended Data Figure 4. Elevated BCL-XL expression in early embryonic epidermis is sufficient to block *Mycn*-dependent apoptotic CC and has no long-term consequence for skin development.

a, Doxycycline-inducible activation of *K14*rtTA by lentivirally-delivered *TRE*-driven transgenes at E12.5 (embryo transduced with *TRE-GFP* is shown, representative of results obtained in two independent litters). **b**, Experimental strategy for elevating BCL-XL expression in the early embryonic epidermis. *TRE-Bcl2l1* was transduced at relatively high titre, whereas CreRFP was transduced at low titre (n=4 embryos). **c**, Whole-mount images of E12.5 transduced embryos show that >50% of basal epidermal cells express BCL-XL and

surround a small population of cells that express both BCL-XL (green) and CreRFP (red). TUNEL (white, signal inverted in right-most image) was quantified (shown in Figure 2a) relative to the position of CreRFP-expressing *Mycn*$^{+/-}$ loser cells that also express BCL-XL. Note that appreciable TUNEL labelling was not observed. Images are representative of data obtained from 2 litters. **d** Differences in proliferation were observed in WT embryos at E12.5 (n=4/genotype) where proliferation was less in BCL-XL^{+} cells compared to controls. At E17.5 there was no difference in proliferation between controls (n=11) and BCL-XL^{+} (n=14; n=number of images analysed from embryos from 2 litters for each genotype, two-sided Mann-Whitney test). **e**, Induction of BCL-XL expression from E9.5 to E15.5 had no appreciable consequence for epidermal differentiation or thickness at E17.5 (control n=54; BCL-XL+ n=68; n=number of thickness measurements taken from images of backskin cryosections from 2 different animals per genotype). Representative images of backskin sections are shown immunolabeled for K14 (green) to mark the basal epidermis, and either K10, Loricrin, Filaggrin (red) to mark the differentiating spinous/granular layers. Dashed lines denote epidermal-dermal border; solid line demarcates the skin surface. Scale bars = 50μm. Data is mean±S.E.M.

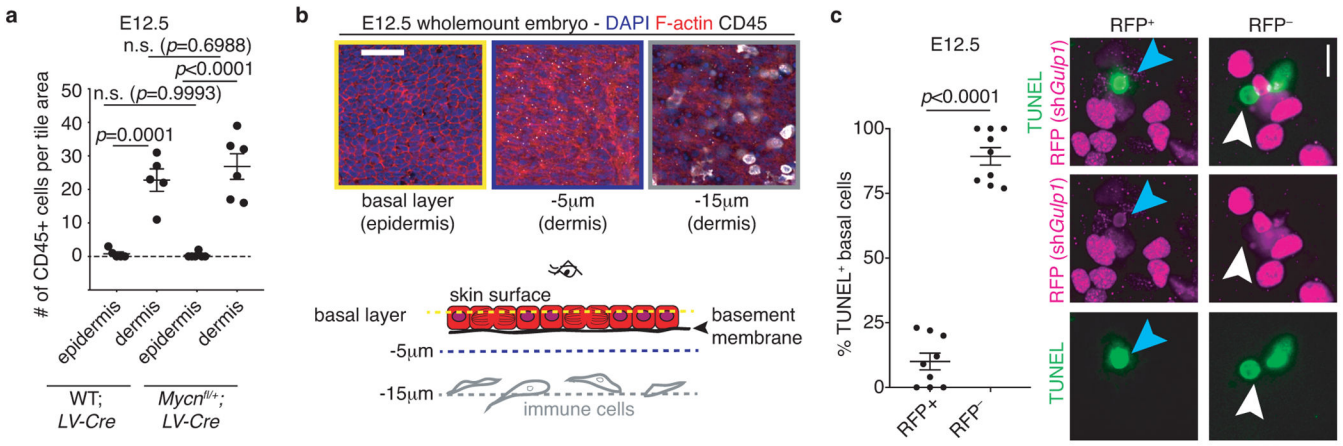

Extended Data Figure 5. Epidermal cells, and not phagocytic immune cells, mediate clearance of corpses at E12.5.

a-b, CD45$^+$ immune cells do not infiltrate the epidermis at E12.5. Wild-type and *Mycn*$^{fl/+}$ embryos were infected with *LV-Cre* at E9.5 and analysed at E12.5. By wholemount immunofluorescence and confocal microscopy, CD45$^+$ immune cells (mostly macrophages at this time) were confined primarily to the deeper dermis. Immune cells were quantified over image tiles that encompassed a region of 425µm x 425µm (n=number of images analysed from 2 embryos per genotype, WT n=5, *Mycn*$^{fl/+}$ n=6, one-way ANOVA with Tukey's multiple comparisons). Representative images from quantifications in **a** are shown in **b** at subsequent z positions within the tissue as indicated. **c,** Few un-cleared cell corpses in *Gulp1* shRNA epidermis are RFP$^+$ suggesting accumulated corpses do not arise simply because of consequences of *Gulp1* knockdown on cell viability. Quantification of RFP status of TUNEL$^+$ corpses in *Gulp1* knockdown epidermis (n=9 images from 4 embryos, two-tailed students t-test). Scale bar= 50µm in **b**; 10µm in **c.** Data is mean±S.E.M.

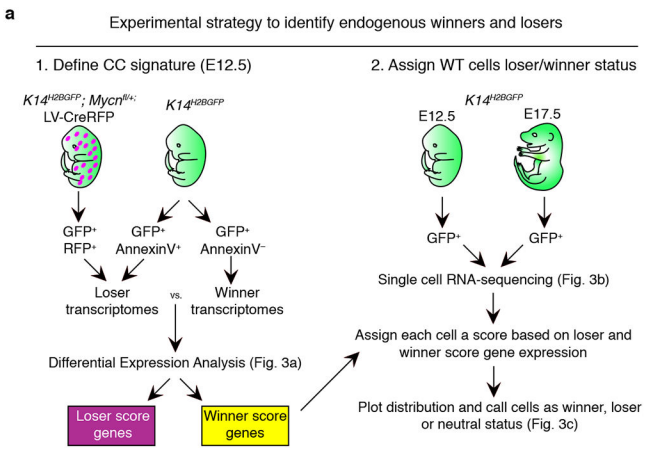

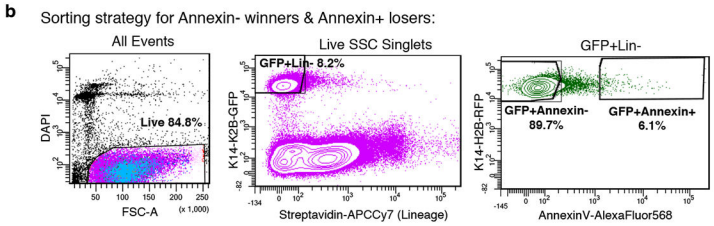

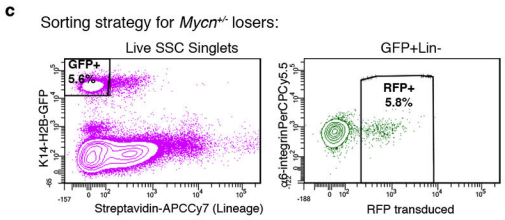

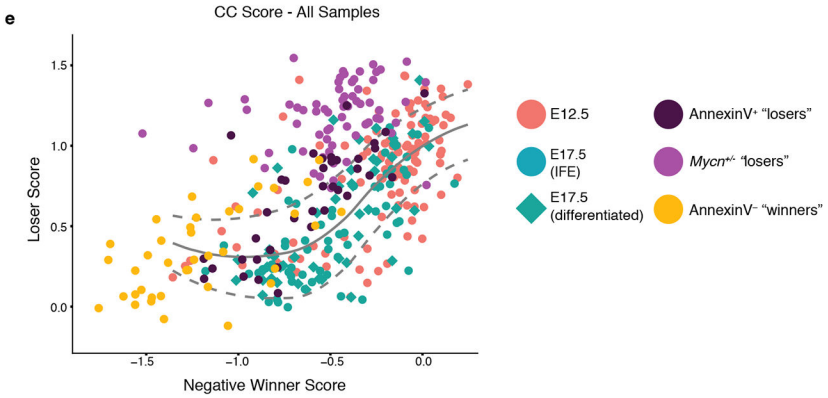

d Genes that define CC Signature (with p-values)

Loser Score Genes

Gene	p_val	avg_logFC	pct.1	pct.2	p_val_adj
mt-Rnr2	2.64E-11	0.6919367	1	1	2.18E-07
Malat1	2.09E-08	0.7783198	1	1	1.73E-04
Gm26905	2.31E-08	0.6092253	0.933	0.487	1.91E-04
6820431F20Rik	2.64E-08	0.5677822	1	0.897	2.18E-04
Gm48415	8.85E-08	0.5618862	0.702	0.308	7.32E-04
Gm48493	1.43E-07	0.8521245	0.75	0.333	1.18E-03
mt-Nd4l	1.44E-07	0.7797485	0.913	0.487	1.19E-03
Socs2	2.27E-07	0.5024792	0.769	0.256	1.87E-03
Gm26624	2.68E-07	0.3429467	0.827	0.385	2.22E-03
mt-Co2	4.24E-07	0.9632147	0.837	0.436	3.51E-03
Kcnq1ot1	6.38E-07	0.6062473	1	0.846	5.28E-03
Alg11	7.67E-07	0.3380907	0.808	0.359	6.35E-03
mt-Co1	7.88E-07	0.4805781	1	1	6.52E-03
Gm47164	1.09E-06	0.5782444	0.942	0.59	9.01E-03
mt-Atp6	1.31E-06	1.0378532	0.865	0.538	1.08E-02
mt-Co3	1.55E-06	0.8554511	0.875	0.513	1.28E-02
Gm48271	2.27E-06	0.5517046	0.923	0.513	1.88E-02
Gm28438	2.45E-06	0.544285	0.942	0.692	2.03E-02
mt-Nd5	2.46E-06	0.6211671	1	1	2.03E-02
Gm37376	4.02E-06	0.6318615	0.952	0.744	3.33E-02
Ptprd	4.03E-06	0.4417884	0.933	0.513	3.33E-02
Alcam	4.59E-06	0.4547163	0.683	0.256	3.79E-02
mt-Nd4	6.01E-06	0.5763139	1	0.923	4.97E-02

Winner Score Genes

Gene	p_val	avg_logFC	pct.1	pct.2	p_val_adj
Rps6-ps4	1.50E-06	-0.4886731	0.135	0.487	1.24E-02
Gm4366	1.10E-06	-0.1907843	0.394	0.667	9.12E-03
Gm10222	2.89E-09	-0.1758947	0.077	0.487	2.39E-05
Gm28661	1.17E-07	-0.1496628	0.212	0.615	9.67E-04
Gm28437	6.89E-07	-.0497043	0.433	0.821	5.70E-03
Gm14303	9.64E-10	-0.991886	0.183	0.667	7.98E-06
Gstp1	2.00E-11	-0.9407164	0.99	1	1.65E-07
Rps16-ps2	5.27E-08	-0.8695387	0.981	0.872	4.36E-04
Gm10443	1.88E-09	-0.8036571	0.269	0.744	1.55E-05
Tuba1b	3.25E-07	-0.7230862	1	1	2.69E-03
Nutf2-ps1	1.45E-06	-0.6957248	0.548	0.821	1.20E-02
Mif	2.23E-07	-0.6713602	1	0.949	1.85E-03
Gm15459	2.56E-06	-0.662973	0.962	0.923	2.12E-02
Gm10260	1.94E-10	-0.6567393	1	1	1.60E-06
Rpl41	4.80E-09	-0.6212474	1	1	3.97E-05
Gm13394	4.06E-11	-0.6203753	1	1	3.36E-07
Gm15772	6.30E-09	-0.6062952	1	1	5.21E-05
Rpl28-ps1	3.75E-09	-0.5478662	1	0.974	3.10E-05
Gm11808	4.95E-06	-0.5256745	0.99	0.897	4.10E-02
Rplp2	6.13E-09	-0.5219023	1	1	5.07E-05
Slva1	3.80E-07	-0.4664276	1	1	3.14E-03
Rps19	4.18E-07	-0.4506147	1	1	3.45E-03
Cox4i1	1.06E-06	-0.3799978	1	1	8.80E-03
Cox8a	1.31E-06	-0.3749392	0.99	1	1.08E-02

Extended Data Figure 6. Generation of a cell competition signature and validation of method to classify wild-type epidermal cells via scRNAseq.

a, Experimental strategy to identify endogenous winners in losers in the epidermis. **b-c,** FACS-based sorting strategies to isolate winners and loser populations from the epidermis. **d**, Differential expression comparing transcriptomes of 39 winner (annexinV^{-}) cells to that of 104 loser (66 *Mycn*$^{+/-}$ and 38 annexinV^{+}) cells uncovers genes that define the CC signature (p-values generated from Wilcoxan rank sum test). Top table: loser genes; bottom table: winner genes. **e**, Putative winners (annexinV^{-}), putative losers (annexinV^{+}), and *Mycn*

$^{+/-}$ losers fall where expected relative to the wild-type distribution based on expression of CC signature genes.

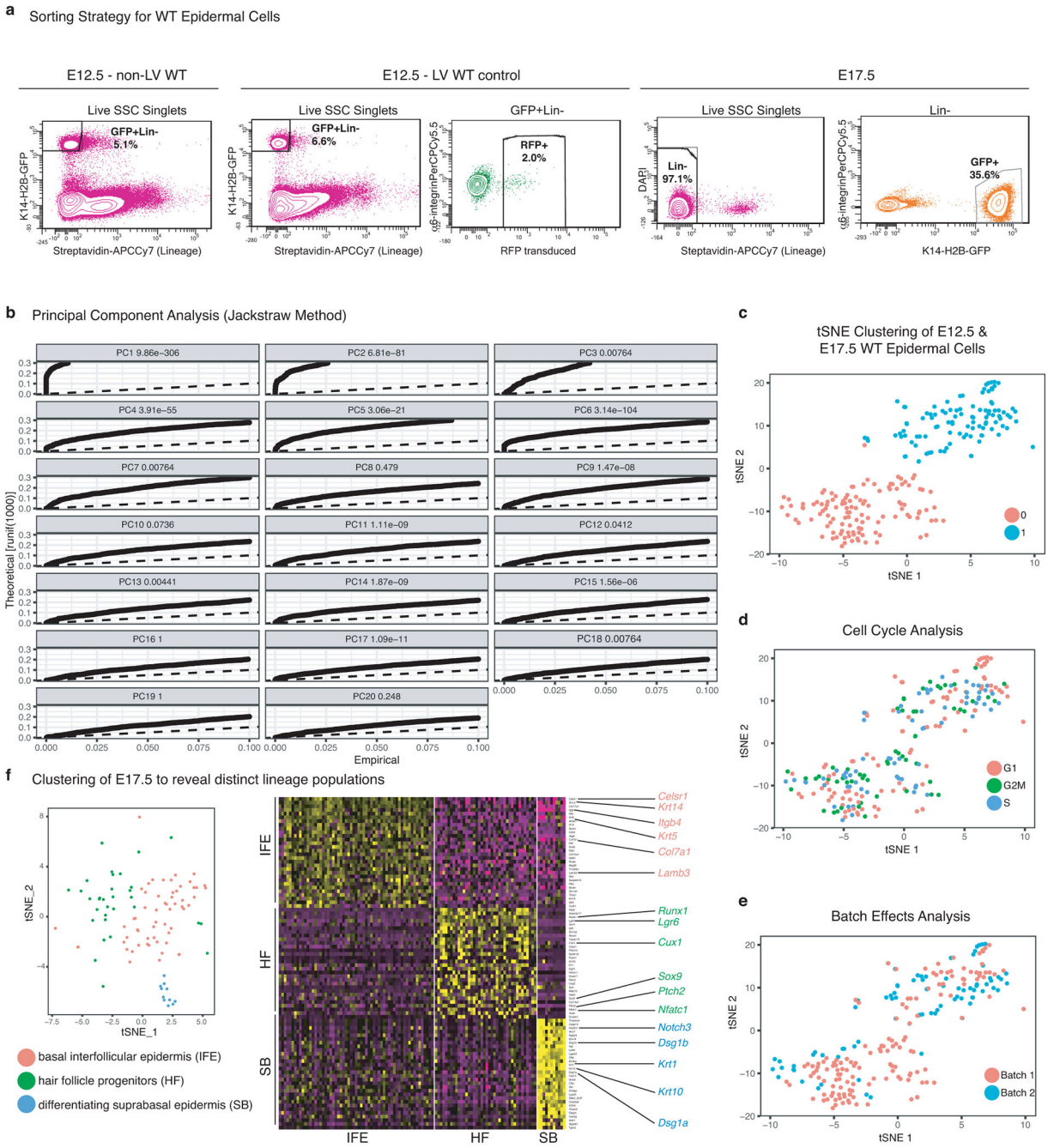

Extended Data Figure 7. scRNA-sequencing of wild-type epidermal cells at E12.5 and E17.5.

a Sorting strategy to isolate WT Epidermal Cells. **b-f** Principal component analysis, **b**, (via the Jackstraw Method, see methods) and tSNE clustering, **c**. Analysis was performed to confirm that neither cell cycle differences (**d**) nor batch effects (**e**) account for the clustering. **f**, Further subclustering of E17.5 cells reveals distinct lineage populations: interfollicular epidermis (IFE), hair follicle (HF), and differentiating suprabasal cells (SB). Analysis was performed on 227 cells (111 E17.5 cells and 116 E12.5 cells). Heatmap shows the top 30 enriched genes defining each cluster.

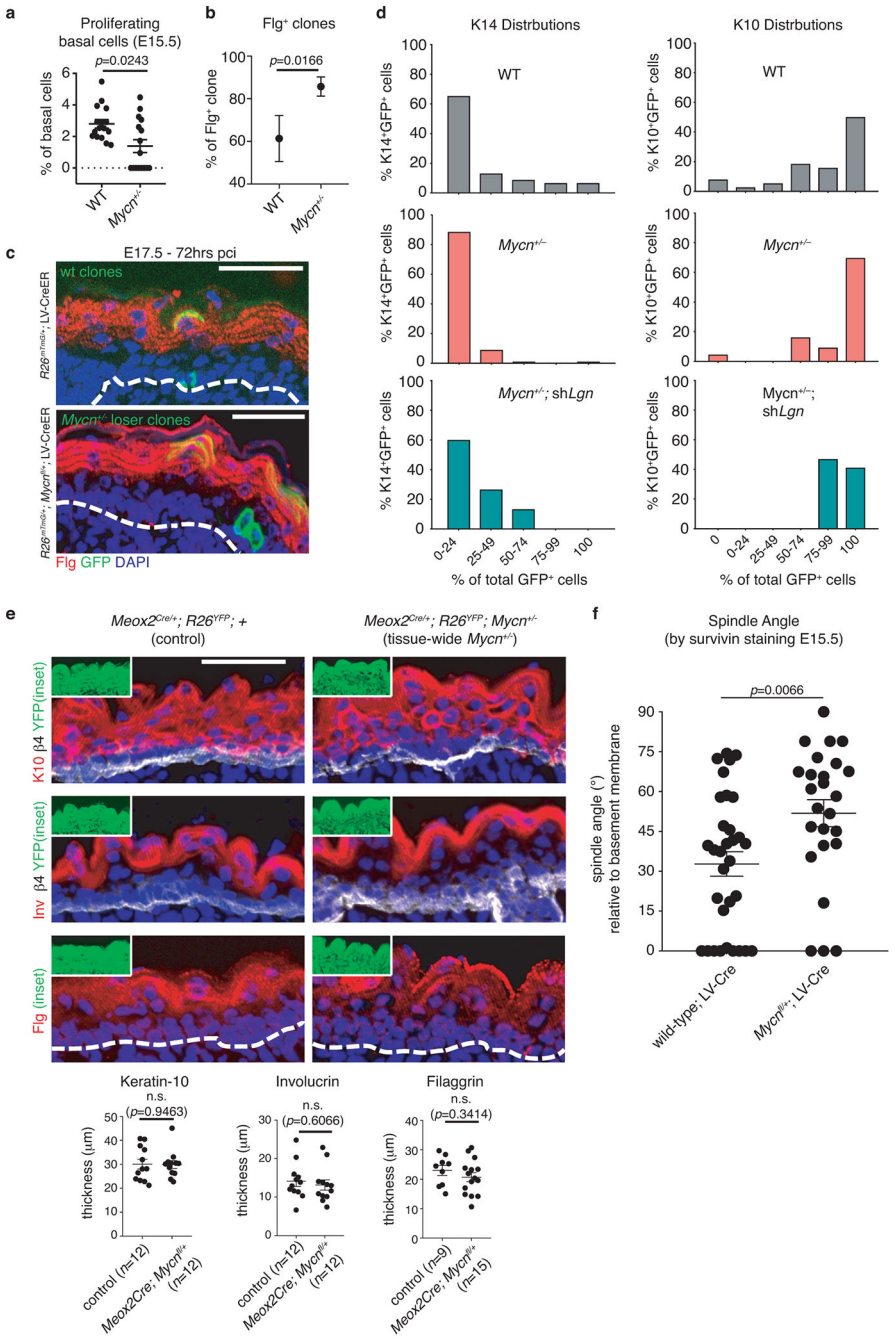

Extended Data Figure 8. Differentiation mediates the context-dependent exit of *Mycn*$^{+/-}$ loser cells from the basal layer during cell competition in late epidermal development.

a, Fewer *Mycn*$^{+/-}$ proliferating basal cells were observed at E15.5 compared to WT neighbours (n= 15 regions measured, two-sided Mann Whitney test). **b-c** *Mycn*$^{+/-}$ losers were more often found in the Flg^{+} layer of the epidermis at E17.5 compared to wild-type control clones (N>10 clones, two-sided Mann-Whitney test). **d**, Binned distributions extracted from data shown in Figure 4c of GFP^{+}K14^{+} clones (left) and GFP^{+},K10^{+} clones (right) for each of three genotypes at E17.5: WT (top, grey), *Mycn*$^{+/-}$ (middle, pink), and

Mycn$^{+/-}$; *shLgn* (bottom, teal). **e**, Tissue-wide loss of one allele of *Mycn* yields no epidermal differentiation phenotypes or evidence of accelerated differentiation. The thickness of the region labelled with 3 different markers of differentiation in the skin (Keratin-10, Involucrin, and Filaggrin) was measured and no significance difference was found between control and *Meox2*^{Cre}; *Mycn*$^{fl/+}$ embryos (n= regions measured from cryosections generated from two different animals per genotype, unpaired two-tailed t-test). *R26*^{YFP} was used as a marker of Cre expression and is shown in the inset. **f**, Spindle angle data from rose diagrams in Figure 4d, plotted as a scatter plot for statistical comparison, WT n=32, *Mycn*$^{+/-}$ n=25, two-sided Mann-Whitney test. Scale bars=50μm. Data is mean ±S.E.M.

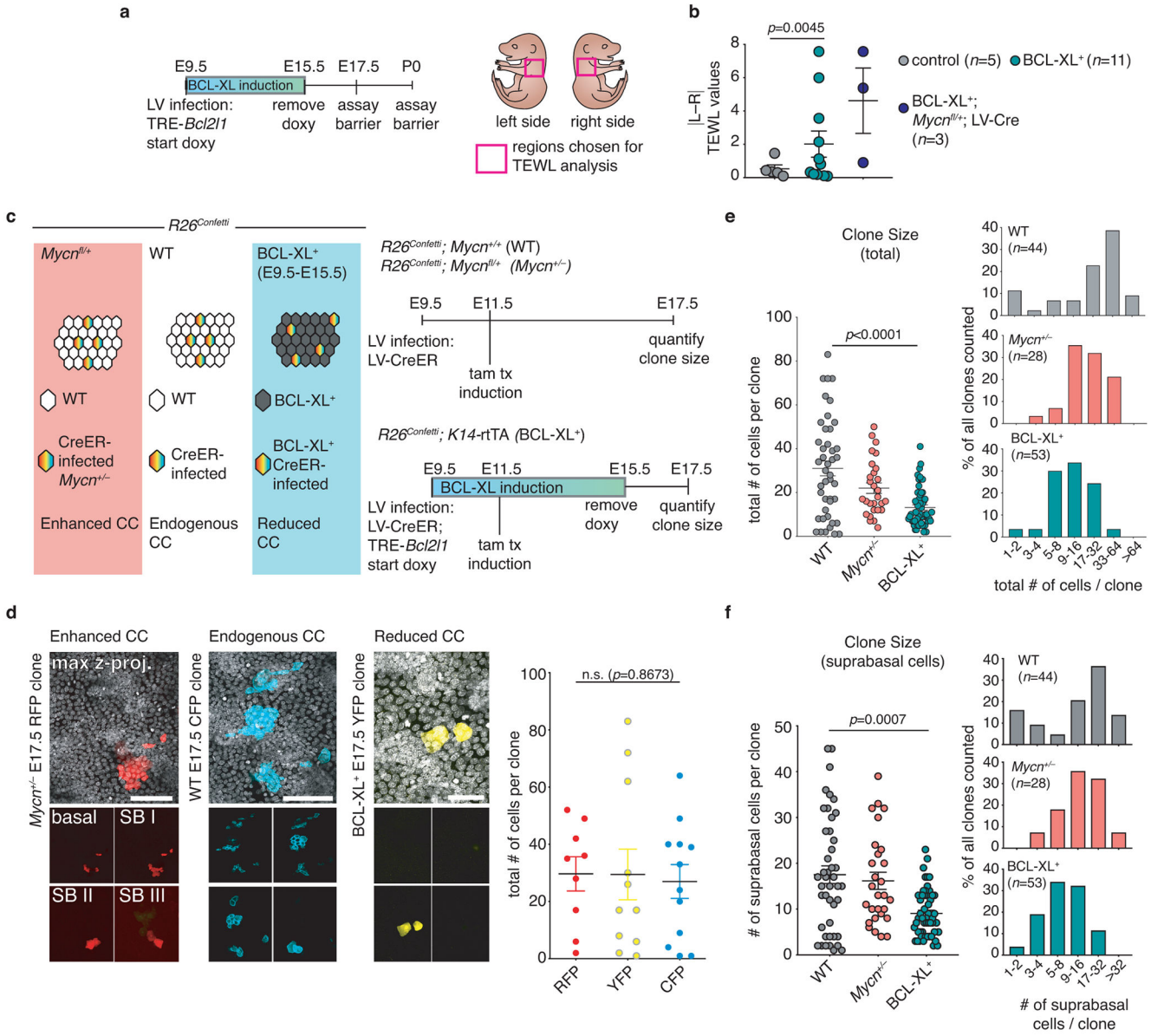

Extended Data Figure 9. Barrier assays and *R26*^{Confetti} labelling experiments uncover functional consequences of disrupting cell competition during epidermal development.

a, Strategy to block apoptotic CC and measure barrier function. **b**, Asymmetry score compares TEWL values from embryo's left and right sides (*n*=number of embryos, F-test to compare variance). **c,** Experimental strategy for confetti lineage tracing. **d** Representative whole-mount images of confetti-marked clones from each genotype at E17.5 (left panels; chosen as examples of clones from 3 litters of embryos analysed for each genotype). Examples of maximum projections and optical sections of individual epidermal layers are shown for each analysed fluor (SB, suprabasal). Quantifications in wild-type embryos (graph at right) show approximately equal labelling efficiency is obtained at E17.5 with each of the 3 confetti fluors (RFP *n*=9 clones, YFP *n*=11 clones, and CFP *n*=12 clones; Kruskal-Wallis

test). **e-f**, Total clone size (**e**) and suprabasal clone size (**f**) dynamics for the genotypes indicated. All data is mean±S.E.M except bar graphs show binned distributions.

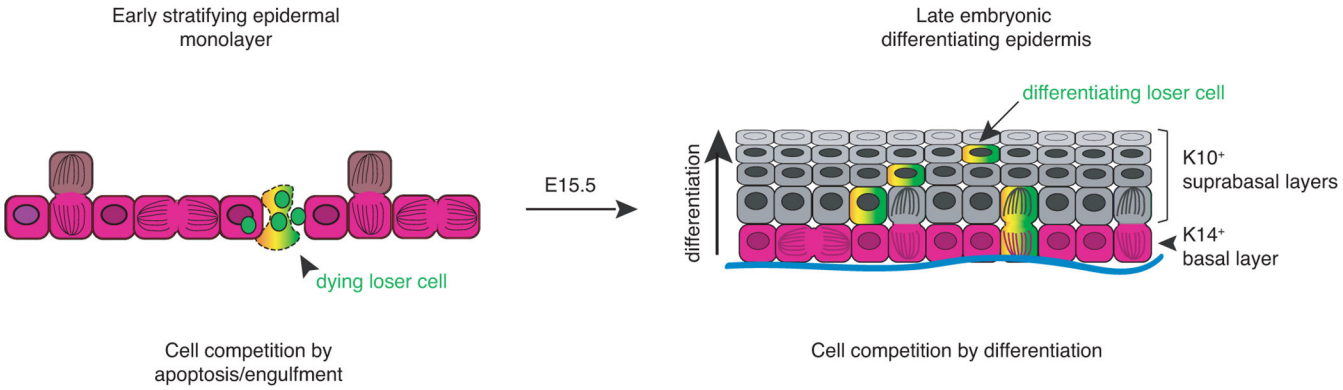

Extended Data Figure 10.

Cartoon schematic illustrating transition in cell competition mechanisms during skin morphogenesis.

Supplementary Material

Refer to Web version on PubMed Central for supplementary material.

Acknowledgements.

We thank I. Matos for assistance with live-imaging set-up and F. García-Quiroz for assistance with TEWL experiments; L. Polak, L. Hidalgo, and M. Sribour for animal assistance; A. Asare for validating *Gulp1* shRNAs; L. Johnston, E. Bach, M. Simunovic, and all Fuchs lab members, but especially M. Laurin, A. Sendoel, S. Baksh, S. Gur-Cohen, S. Liu, and K. Stewart for discussion and/or comments on the manuscript. We thank Rockefeller University (RU) Bio-Imaging Resource Center for use of microscopes, RU Comparative Bioscience Center (AAALAC-accredited) for care of mice in accordance with National Institutes of Health (NIH) guidelines, and RU Flow Cytometry Resource Center for assistance with FACS. SJE was supported by fellowships from the Human Frontiers Science Program (LT000907/2015) and RU Women & Science. NCG holds a Burroughs Wellcome Fund Postdoctoral Enrichment Program Award and an NIH Postdoctoral Ruth L. Kirschstein National Research Service Award F32CA221353. AFM was supported by an Arnold O. Beckman Postdoctoral Fellowship. YG is supported by a NIAMS 1K01AR072132–01A1 Career Development Award and an Irene Diamond Fund/AFAR Postdoctoral Transition Awards in Aging. EF is an HHMI Investigator. This research was supported by NIH (R01-AR27883 to EF).

References:

1. Morata G & Ripoll P Minutes: Mutants of Drosophila autonomously affecting cell division rate. Dev. Biol 42, 211–221 (1975). [PubMed: 1116643]
2. Simpson P & Morata G Differential mitotic rates and patterns of growth in compartments in the Drosophila wing. Dev. Biol. 85, 299–308 (1981). [PubMed: 7262460]
3. Simpson P Parameters of cell competition in the compartments of the wing disc of Drosophila. Dev. Biol. 69, 182–193 (1979). [PubMed: 446891]
4. Moreno E, Basler K & Morata G Cells compete for decapentaplegic survival factor to prevent apoptosis in Drosophila wing development. Nature 416, 755–759 (2002). [PubMed: 11961558]
5. Johnston LA, Prober DA, Edgar BA, Eisenman RN & Gallant P Drosophila myc regulates cellular growth during development. Cell 98, 779–790 (1999). [PubMed: 10499795]
6. De La Cova C, Abril M, Bellosta P, Gallant P & Johnston LA Drosophila myc regulates organ size by inducing cell competition. Cell 117, 107–116 (2004). [PubMed: 15066286]
7. Rhiner C et al. Persistent competition among stem cells and their daughters in the Drosophila ovary germline niche. Development 136, 995–1006 (2009). [PubMed: 19211674]

8. Stine RR, Greenspan LJ, Ramachandran KV & Matunis EL Coordinate regulation of stem cell competition by Slit-Robo and JAK-STAT in signaling in the Drosophila testis. PLoS Genet. 10, e1004713 (2014). [PubMed: 25375180]
9. Amoyel M, Simons BD & Bach EA Neutral competition of stem cells is skewed by proliferative changes downstream of Hh and Hpo. EMBO J. 33, 2295–2313 (2014). [PubMed: 25092766]
10. Clavería C & Torres M Cell Competition: Mechanisms and Physiological Roles. Annu. Rev. Cell Dev. Biol. 32, 411–439 (2016). [PubMed: 27501445]
11. Di Gregorio A, Bowling S & Rodriguez TA Cell Competition and Its Role in the Regulation of Cell Fitness from Development to Cancer. Developmental Cell 38, 621–634 (2016). [PubMed: 27676435]
12. Clavería C, Giovinazzo G, Sierra R & Torres M Myc-driven endogenous cell competition in the early mammalian embryo. Nature 500, 39–44 (2013). [PubMed: 23842495]
13. Díaz-Díaz C et al. Pluripotency Surveillance by Myc-Driven Competitive Elimination of Differentiating Cells. Dev. Cell 42, 585–599.e4 (2017). [PubMed: 28919206]
14. Sancho M et al. Competitive interactions eliminate unfit embryonic stem cells at the onset of differentiation. Dev. Cell 26, 19–30 (2013). [PubMed: 23867226]
15. Kon S et al. Cell competition with normal epithelial cells promotes apical extrusion of transformed cells through metabolic changes. Nat. Cell Biol. 19, 530–541 (2017). [PubMed: 28414314]
16. Martins VC et al. Cell competition is a tumour suppressor mechanism in the thymus. Nature 509, 465–470 (2014). [PubMed: 24828041]
17. Bondar T & Medzhitov R p53-mediated hematopoietic stem and progenitor cell competition. Cell Stem Cell 6, 309–322 (2010). [PubMed: 20362536]
18. Moreno E & Basler K dMyc transforms cells into super-competitors. Cell 117, 117–129 (2004). [PubMed: 15066287]
19. Asare A, Levorse J & Fuchs E Coupling organelle inheritance with mitosis to balance growth and differentiation. Science 355, eaah4701 (2017). [PubMed: 28154022]
20. Beronja S, Livshits G, Williams S & Fuchs E Rapid functional dissection of genetic networks via tissue-specific transduction and RNAi in mouse embryos. Nat. Med. 16, 821–827 (2010). [PubMed: 20526348]
21. Tallquist MD & Soriano P Epiblast-restricted Cre expression in MORE mice: A tool to distinguish embryonic vs. extra-embryonic gene function. Genesis 26, 113–115 (2000). [PubMed: 10686601]
22. Mesa KR et al. Niche-induced cell death and epithelial phagocytosis regulate hair follicle stem cell pool. Nature 522, 94–97 (2015). [PubMed: 25849774]
23. Tirosh I et al. Dissecting the multicellular ecosystem of metastatic melanoma by single-cell RNA-seq. Science 352, 189–196 (2016). [PubMed: 27124452]
24. Fuchs E Scratching the surface of skin development. Nature 445, 834–842 (2007). [PubMed: 17314969]
25. Williams SE, Beronja S, Pasolli HA & Fuchs E Asymmetric cell divisions promote Notch-dependent epidermal differentiation. Nature 470, 353–358 (2011). [PubMed: 21331036]
26. Williams SE, Ratliff LA, Postiglione MP, Knoblich JA & Fuchs E Par3-mInsc and Gα i3 cooperate to promote oriented epidermal cell divisions through LGN. Nat. Cell Biol. 16, 758–769 (2014). [PubMed: 25016959]
27. Segre JA, Bauer C & Fuchs E Klf4 is a transcription factor required for establishing the barrier function of the skin. Nat. Genet. 22, 356–360 (1999). [PubMed: 10431239]
28. Indra AK & Leid M Epidermal permeability barrier measurement in mammalian skin. Methods Mol. Biol. 763, 73–81 (2011). [PubMed: 21874444]
29. Lee CH et al. A Regulatory Response to Ribosomal Protein Mutations Controls Translation, Growth, and Cell Competition. Dev. Cell 24, 456–469 (2018).
30. Merino MM et al. Elimination of unfit cells maintains tissue health and prolongs lifespan. Cell 160, 461–476 (2015). [PubMed: 25601460]
31. Lynch MD et al. Spatial constraints govern competition of mutant clones in human epidermis. Nat. Commun 8, 1119 (2017). [PubMed: 29066762]

32. Martincorena I et al. High burden and pervasive positive selection of somatic mutations in normal human skin. Science 348, 880–886 (2015). [PubMed: 25999502]

33. Brown S et al. Correction of aberrant growth preserves tissue homeostasis. Nature 548, 334–337 (2017). [PubMed: 28783732]

Methods References:

34. Muzumdar MD, Tasic B, Miyamichi K, Li N & Luo L A global double-fluorescent cre reporter mouse. Genesis 45, 593–605 (2007). [PubMed: 17868096]

35. Snippert HJ et al. Intestinal crypt homeostasis results from neutral competition between symmetrically dividing Lgr5 stem cells. Cell 143, 134–144 (2010). [PubMed: 20887898]

36. Knoepfler PS, Cheng PF & Eisenman RN N- myc is essential during neurogenesis for the rapid expansion of progenitor cell populations and the inhibition of neuronal differentiation. Genes Dev. 16, 2699–2712 (2002). [PubMed: 12381668]

37. Srinivas S et al. Cre reporter strains produced by targeted insertion of EYFP and ECFP into the ROSA26 locus. BMC Dev. Biol. 1, 4 (2001). [PubMed: 11299042]

38. Ouspenskaia T, Matos I, Mertz AF, Fiore VF & Fuchs E WNT-SHH Antagonism Specifies and Expands Stem Cells prior to Niche Formation. Cell 164, 156–169 (2016). [PubMed: 26771489]

39. Picelli S et al. Smart-seq2 for sensitive full-length transcriptome profiling in single cells. Nat. Methods 10, 1096–1098 (2013). [PubMed: 24056875]

40. Patro R, Duggal G, Love MI, Irizarry RA & Kingsford C Salmon provides fast and bias-aware quantification of transcript expression. Nat. Methods 14, 417–419 (2017). [PubMed: 28263959]

41. Soneson C, Love MI & Robinson MD Differential analyses for RNA-seq: transcript-level estimates improve gene-level inferences. F1000Research 4, 1521 (2016).

42. Brennecke P et al. Accounting for technical noise in single-cell RNA-seq experiments. Nat. Methods 10, 1093–1095 (2013). [PubMed: 24056876]

43. Butler A, Hoffman P, Smibert P, Papalexi E & Satija R Integrating single-cell transcriptomic data across different conditions, technologies, and species. Nat. Biotechnol. 36, 411–420 (2018). [PubMed: 29608179]

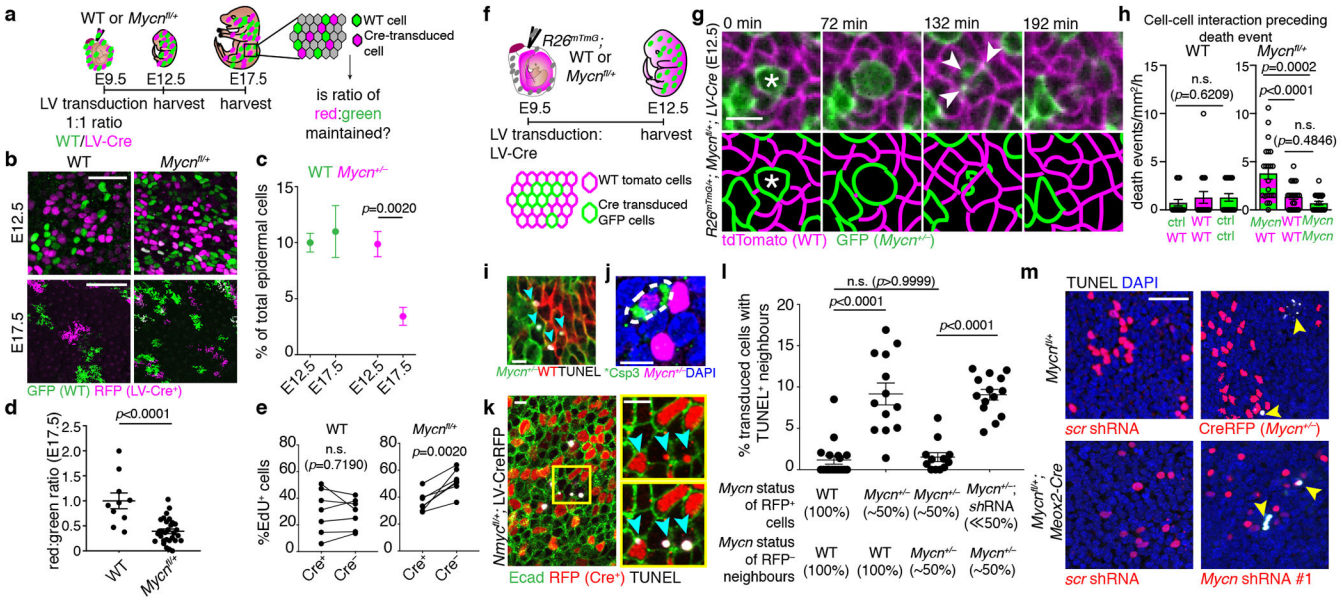

Figure 1. Cell competition occurs in the developing mouse epidermis.

a-d Comparative growth assay strategy (**a**) and representative whole-mount images (**b,** similar results obtained with 2 independent biological replicates) reveal representation of RFP$^+$Cre$^+$ (magenta) and GFP$^+$ wild-type (green) cells in the epidermis at E12.5 (n=2 embryos/genotype) and E17.5 (**c**, n=3 embryos/genotype, two-tailed unpaired t-test). Ratios of RFP$^+$ to GFP$^+$ cells after normalizing initial representations in each genotype (**d**, WT n=10 images, *Mycn*$^{fl/+}$ n=30, measurements made from 2 litters per genotype, 2-tailed unpaired t-test). **e** EdU incorporation assay (n=7 regions measured from 3 embryos/genotype obtained from 2 independent litters, two-tailed paired t-test). **f-h** Death events from E12.5 time-lapse images quantified and binned by neighbour-neighbour interaction categories (WT n=18 videos, 2 embryos; *Mycn*$^{fl/+}$ n=22 videos, 3 embryos, one-way ANOVA with Tukey's multiple comparisons test). Still images (**g**) from a video capturing a representative death of a *Mycn*$^{+/-}$ cell (asterisk) in contact with wild-type neighbours. Bottom panel: segmented image traces. **i** TUNEL$^+$-fragments (white) accumulate along boundaries of wild-type (red) and *Mycn*$^{+/-}$ (green) cells; image representative of 5 independent experiments. **j** Activated caspase-3 expression (green) captured within a dying E12.5 RFP$^+$*Mycn*$^{+/-}$ cell (magenta); image representative of 2 independent experiments. **k,** TUNEL$^+$RFP$^+$ corpses within 3 cell-lengths of CreRFP$^+$ cells at E12.5. **l-m,** Quantifications and representative images of neighbouring TUNEL$^+$ corpses (data obtained from 2 litters, 2–4 measurements were made per embryo, n=number of images analysed, WT/WT n=18, WT/*Mycn*$^{fl/+}$ n=13, *Mycn*$^{fl/+}$/ *Mycn*$^{fl/+}$ n=12, *Mycn*$^{fl/+}$/ *Mycn*$^{fl/+}$; sh*Mycn* n=14, Kruskal-Wallis test with Dunn's multiple comparisons). All arrowheads denote apoptotic bodies. Scale bars=50μm with the following exceptions: in **b**, bottom panel=500μm; in g,i-k=10μm; all data=mean ±S.E.M.

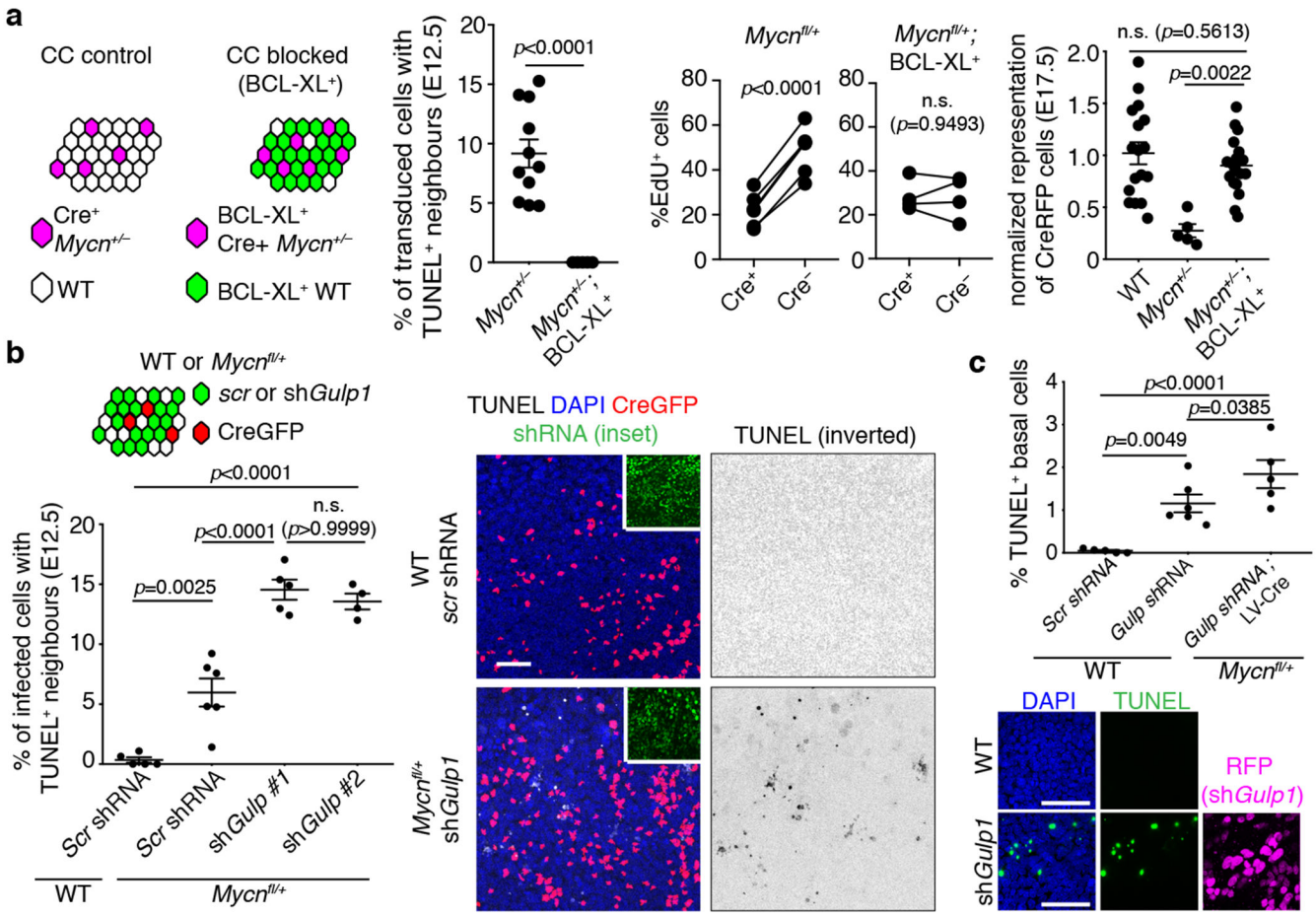

Figure 2. Cell competition involves apoptosis and epidermal engulfment of dying cells.

a BCL-XL over-expression in *Mycn*$^{+/-}$ mosaics. TUNEL (*n*=number of images analysed, *Mycn*$^{fl/+}$ *n*=11, *Mycn*$^{fl/+}$; BCL-XL^{+} *n*=5, two-sided Mann-Whitney test) and EdU incorporation assays (*n*=number of images analysed, *Mycn*$^{fl/+}$ *n*=6, *Mycn*$^{fl/+}$; BCL-XL^{+} *n*=5, two-tailed paired t-test) were performed at E12.5. Comparative growth assays at E17.5 (*n*=number of images analysed from 2 litters per genotype, WT *n*=17, *Mycn*$^{fl/+}$;BCL-XL^{+} *n*=19, *Mycn*$^{fl/+}$ *n*=5, one-way ANOVA with Tukey's multiple comparisons). **b-c** TUNEL quantifications relative to RFP^{+} cells (**b**) or throughout basal epidermis (**c**) in wild-type and *Mycn*$^{+/-}$ E12.5 embryos transduced with *LV-Cre* and *scr-shRNA* or *Gulp1* shRNA (*n*=number of images analysed, obtained from 2 independent litters per genotype; **b,** WT/sh*Scr* *n*=5; *Mycn*$^{fl/+}$/sh*Scr* *n*=6; *Mycn*$^{fl/+}$/sh*Gulp* #1 *n*=5; *Mycn*$^{fl/+}$/sh*Gulp1 #2;* **c,** *n*=4,WT/sh*Scr* *n*=5; WT/sh*Gulp* *n*=6; *Mycn*$^{fl/+}$/sh*Gulp1* *n*=5; statistical tests: one-way ANOVA with Bonferroni's multiple comparisons). Representative images are shown; TUNEL signals are inverted in **b**. Scale bars: **b-c**, 50μm; Data=mean ±S.E.M.

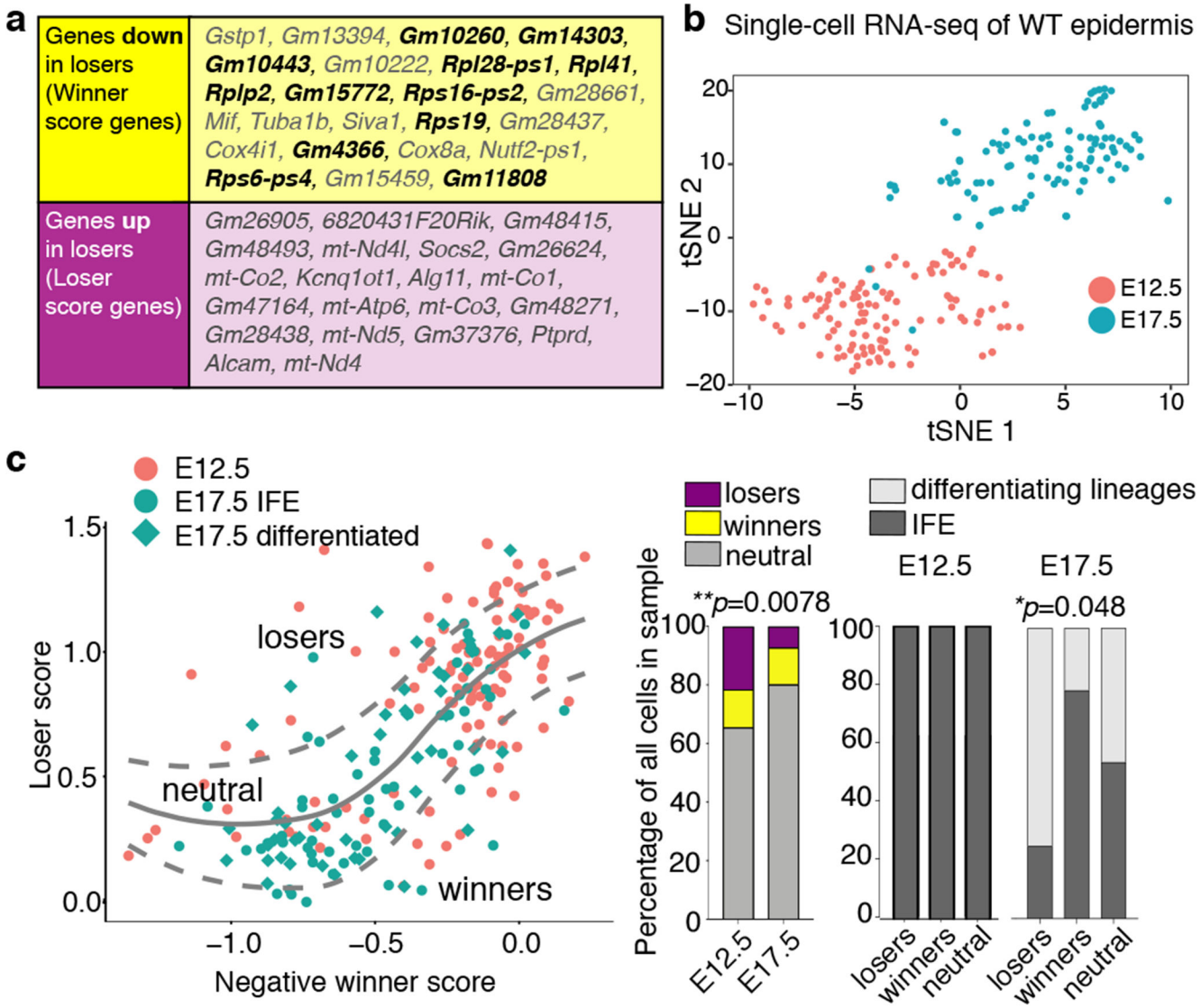

Figure 3. Single-cell RNA sequencing reveals a transcriptional signature for CC and suggests endogenous CC is active during epidermal development.

a, Winner and loser score genes uncovered by differential expression analysis. Ribosomal genes are in bold. **b** tSNE clustering of wild-type epidermal cells (E12.5 n=116; E17.5 n=111) following single-cell RNA-sequencing. **c** Wild-type cells were assigned a score based on expression of CC signature genes and resulting distribution was fit via a LOESS Regression (left panel). Outliers (>1 standard deviation) were called as losers or winners (middle panel; χ^2-test, **p=0.0078). Losers/winners/neutral cells were further classified according to transcriptional identity within epidermal compartments at E17.5 (right panel, χ^2-test, *p=0.0474).

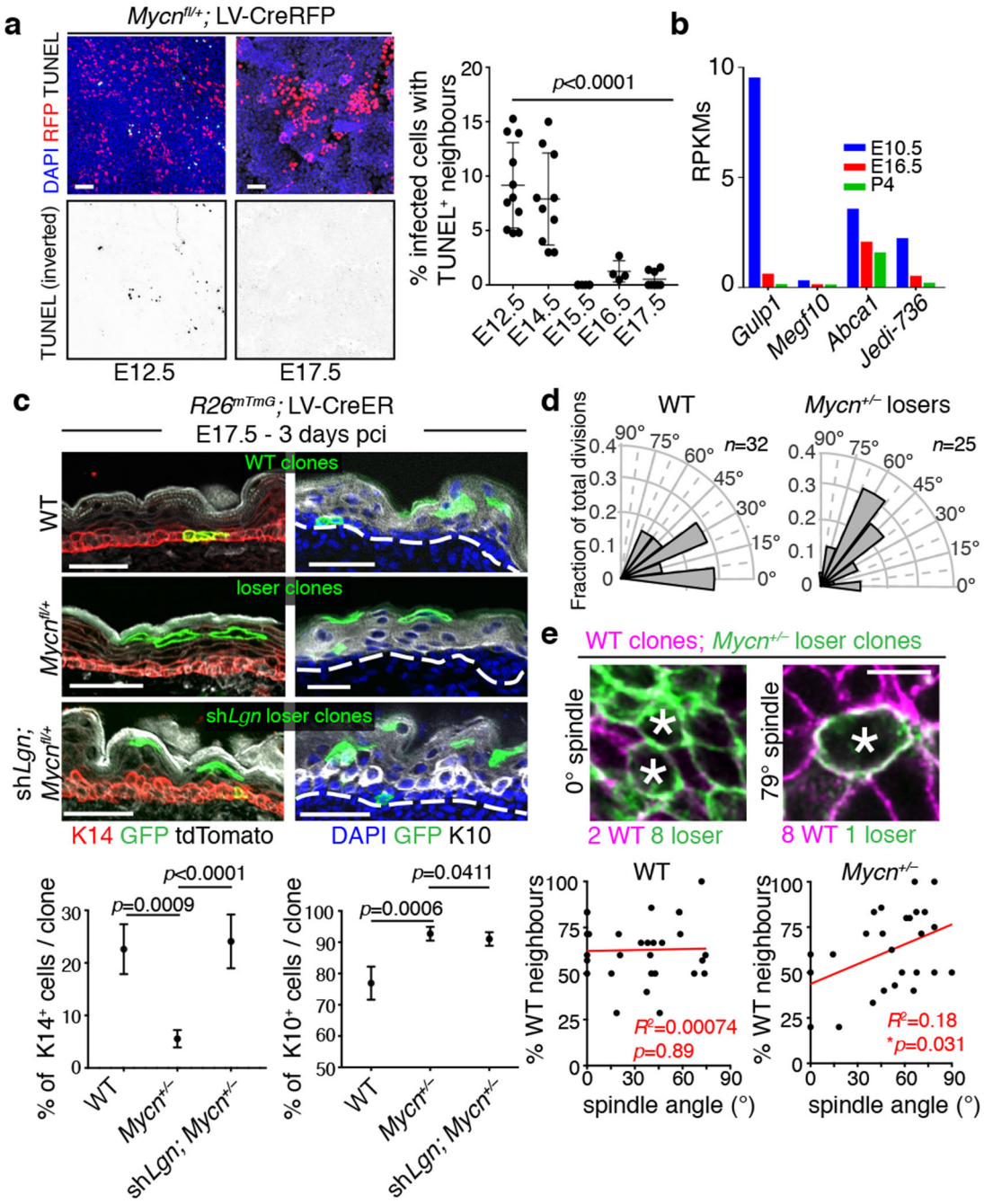

Figure 4. A shift in CC-induced loser cell elimination mechanisms concomitant with epidermal stratification and maturation.

a, Quantification of TUNEL neighbouring *Mycn*$^{+/-}$ clones and representative wholemount images from E12.5→E17.5 (*n*=number of images quantified from 2 independent litters per time point, E12.5 *n*=11, E14.5, *n*=10, E15.5 *n*=6, E16.5 *n*=4, E17.5 *n*=8, Kruskal-Wallis test with Dunn's multiple comparisons). **b**, Developmental expression profile of engulfment genes in epidermal progenitors **c**, Representative sagittal images and quantifications of E17.5 backskins to assess K14^{+} labelling (WT *n*=46 clones, *Mycn*$^{+/-}$ *n*=88 clones, *Mycn*

$^{+/-}$;sh*Lgn* *n*=15 clones, Kruskal-Wallis test with Dunn's multiple comparisons), and K10^{+} labelling (WT *n*=38 clones, *Mycn*$^{+/-}$ *n*=80 clones, *Mycn*$^{+/-}$;sh*Lgn* *n*=17 clones, Kruskal-Wallis test with Dunn's multiple comparisons). **d** Quantification of spindle angle relative to the basement membrane (*n*=number of dividing GFP^{+} clones scored from 3 WT embryos and 4 *Mycn*$^{fl/+}$ embryos collected from 2 independent litters). **e,** Correlation analysis between spindle angle (*x*-axis) of GFP^{+} cells and number of RFP^{+} neighbours (*y*-axis) for wild-type (left) and *Mycn*$^{+/-}$ (right) GFP^{+} cells. Representative image (from 4 embryos analysed) of a GFP^{+}*Mycn*$^{+/-}$ loser surrounded largely by other losers dividing within the basal plane (left image), whereas a *Mycn*$^{+/-}$ loser surrounded by mostly wild-type (Tomato^{+}) cells divides at a more perpendicular angle (right image). Scale bars: **a**=250μm; **c**=50μm, **e**=10μm. Data: mean ±S.E.M.

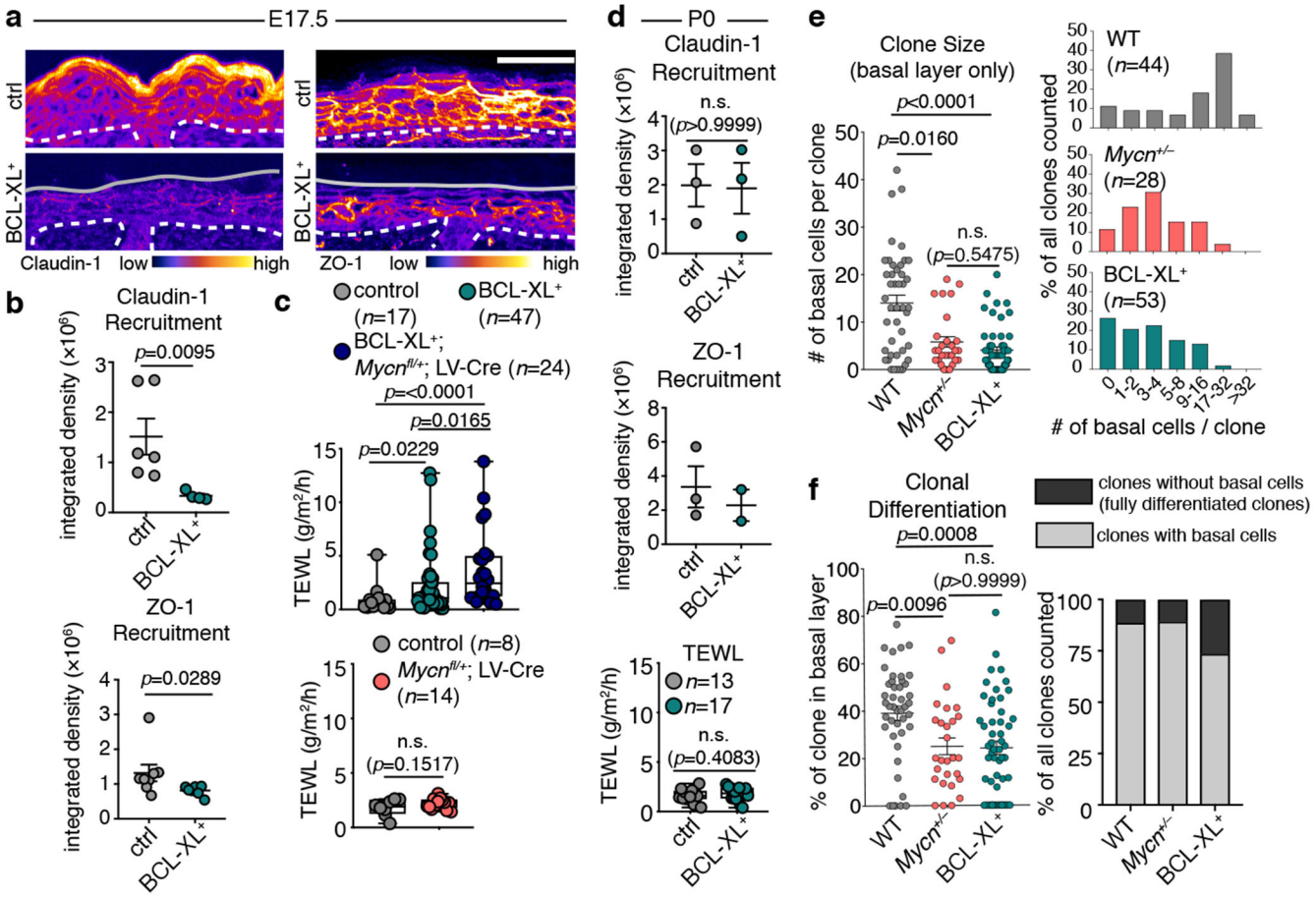

Figure 5. Consequences of CC for epidermal barrier function and clonal dynamics.

a-b, Representative images (**a**) and quantification (**b**) of TJ components Claudin-1 (WT *n*=6, BCL-XL$^+$ *n*=4) and ZO-1 (WT *n*=8, BCL-XL$^+$ *n*=7) recruitment in control and BCL-XL$^+$ embryos at E17.5 (*n*=number of images from 2 different animals per genotype, two-tailed Mann Whitney Test). **c** TEWL measurements at E17.5 for control or BCL-XL$^+$ embryos with/without *Mycn*$^{+/-}$ losers compared to controls (*n*=TEWL measurements obtained from all embryos in 2 litters per genotype, statistical tests: Kruskal-Wallis Test with Dunn's multiple comparisons; bottom plot, two-tailed Mann Whitney Test). **d**. TJ component recruitment and TEWL measurements at P0 (differences assessed via two-tailed Mann Whitney Test). **e-f** Quantifications at E17.5 of basal cells per clone (**e**) and extent of differentiation (% basal cells within clone; **f**). Scatter plots show raw data; bar graphs show binned distributions. Differences from wild-type distributions assessed via Kruskal-Wallis tests, *n*=number of clones counted from 3 litters per genotype, WT *n*=44, *Mycn*$^{+/-}$ *n*=28, BCL-XL$^+$ *n*=53. Scale bars=50μm. TEWL data=median±interquartile range (box), minima/maxima (whiskers); all other data=mean±S.E.M.